Karlsruhe Institute of Technology

wave phenomena
analysis and numerics

Inverse electromagnetic scattering problems for long tubular objects

Tilo Arens, Marvin Knöller, Raphael Schurr

CRC Preprint 2024/17, August 2024

KARLSRUHE INSTITUTE OF TECHNOLOGY

CRC 1173

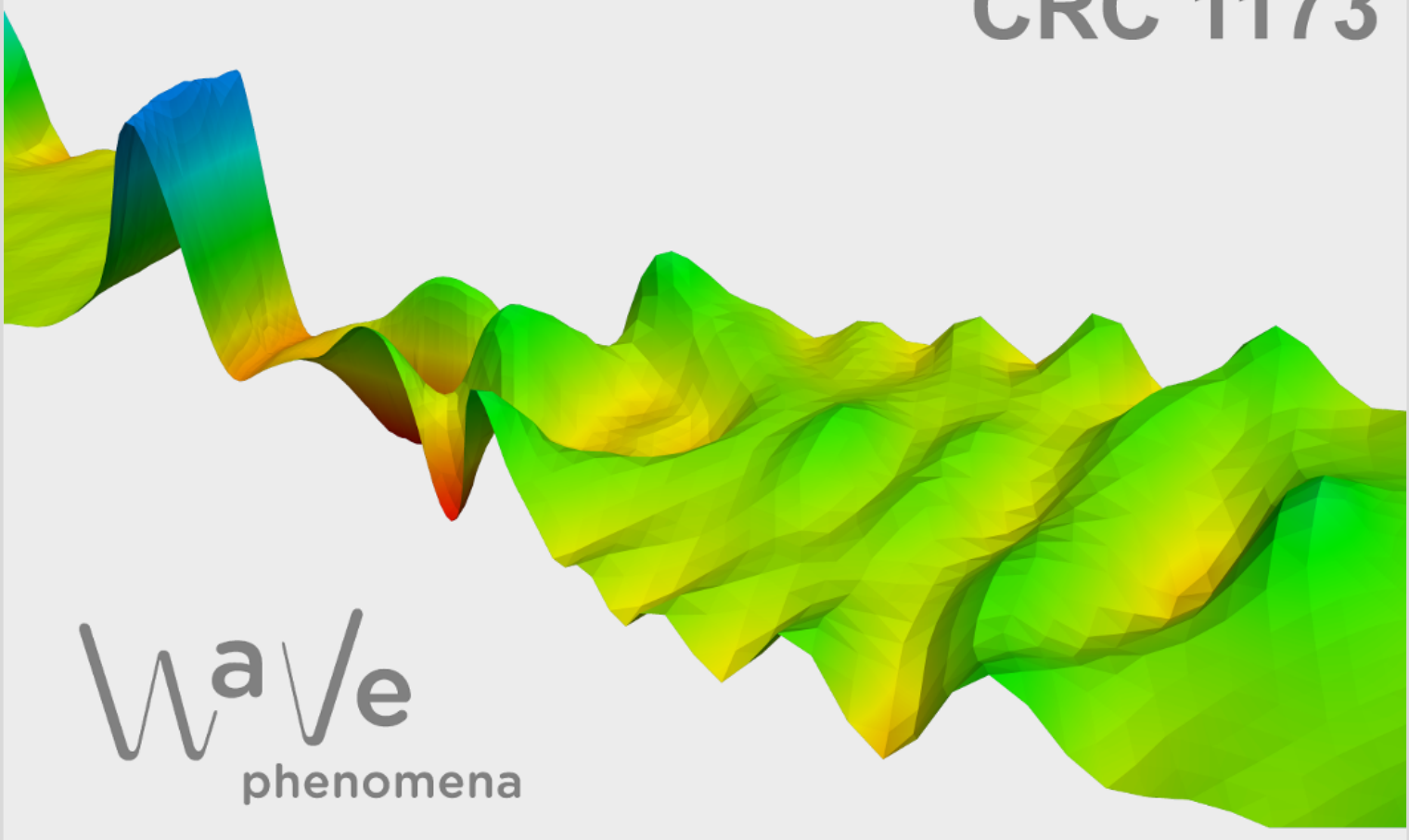

Participating universities

Funded by

ISSN 2365-662X

Inverse Electromagnetic Scattering Problems for Long Tubular Objects

Tilo Arens* Marvin Knöller† Raphael Schurr‡

August 22, 2024

Abstract

We consider the inverse time-harmonic electromagnetic scattering problem of reconstructing an object from knowledge of the generated far field pattern for one incident field in the case of a long tubular object. Both perfectly conducting and penetrable objects are considered. The inverse scattering problem can be formulated as a non-linear, ill-posed operator equation, where the operator is the far field map that maps the boundary of the scatterer to the far field pattern of the scattered field. The shape of the scatterer is reconstructed using a Gauss–Newton minimization procedure for the regularized relative residual of this equation. Our main theoretical result is a characterization of the domain derivative of the far field map for the class of tubular objects considered. Numerical examples are provided in which the computation of the electromagnetic scattered fields and their domain derivatives are carried out using boundary element methods. Even for noisy data we obtain very accurate reconstructions of scatterers with rather complicated shapes.

Keywords: inverse scattering, Maxwell's equations, shape derivative, tubular objects

MSC codes: 35R30, 78A46

1 Introduction

In this paper, we are concerned with the scattering of time-harmonic electromagnetic waves by a perfectly conducting or penetrable obstacle. Motivated by applications in the design of highly chiral scatterers [7–10], we consider tubular objects, in particular, those having a helical structure. We derive a computable characterization of the domain derivative of the far field map for such objects and numerically solve the inverse problem of reconstructing such objects from far field data for one incident field through a regularized iterative Gauss–Newton scheme.

Tubular scatterers have previously been considered in a series of papers [1, 5, 8] in the case of a very small cross section. In this case, asymptotic representation formulas for the scattered electromagnetic field and the derivative of the resulting far field with respect to variations of the curve have been derived and used in algorithms for finding such objects from far field data and optimizing the center curve in order to maximize electromagnetic chirality. However, the objects

*Institut für Angewandte und Numerische Mathematik, Karlsruher Institut für Technologie, Englerstr. 2, 76131 Karlsruhe, Germany tilo.arens@kit.edu

†Institut für Angewandte und Numerische Mathematik, Karlsruher Institut für Technologie, Englerstr. 2, 76131 Karlsruhe, Germany marvin.knoeller@kit.edu

‡Institut für Angewandte und Numerische Mathematik, Karlsruher Institut für Technologie, Englerstr. 2, 76131 Karlsruhe, Germany raphael.schurr@kit.edu

arising via this approach have turned out to be difficult to realize in practice due to their extremely thin nature. Thus, there is a need to develop shape optimization procedures for thicker tubular objects. It is our ultimate aim to generalize the results obtained using asymptotic representation formulas to the more general class of obstacles considered here. Characterizing the domain derivative and solving the inverse scattering problem is a first step in this direction.

The principal approach to solving an inverse scattering problem by an iterative algorithm of Gauss–Newton type is well-established, see [15] and the references contained therein. Given an incident field, one studies the dependence of the scattered field or its far field pattern on variations of the boundary of the scatterer. Considering an abstract far field map that maps the boundary of the obstacle onto the far field of the scattered field, one needs to establish existence of the map's Fréchet derivative as well as a characterization of this derivative that allows its computation in numerical algorithms.

We base our work on the existence proofs and characterization of the domain derivative of the electromagnetic far field established in [13, 19] for perfectly conducting and in [14] for penetrable scatterers. By using a representation of the boundary of the scatterer by a parametrization involving functions from a suitably chosen function space, one may consider the far field map as an operator mapping (a subset of) a normed space to the space of far field patterns. In previously published realizations of this approach [12], star-shaped objects were considered. This assumption renders the dependence of the boundary parameterization on functions in the domain of the far field map linear. This substantially simplifies both the characterization of the domain derivative as well as the implementation of the numerical algorithm. In contrast, the tubular domains considered here have a non-linear dependence of their boundary parametrizations on the functions in the domain of the far field map. A careful analysis of their linearizations yields both explicit expressions for all terms in the domain derivative characterization as well as the theoretical arguments to apply the previously established existence results.

Our work is limited to the case of a homogeneous, isotropic exterior medium, and, in the case of a penetrable obstacle, we will also assume that the material inside the scatterer is homogeneous and isotropic. This allows us to formulate equivalent boundary integral equations for the scattering problems which may be solved by the boundary element method. We note that for both the perfect conductor and the penetrable medium problem, the domain derivative for the scattered far field is characterized by an exterior boundary value problem of the same structure as the original scattering problem. Thus, in either case the same boundary integral equation formulation may be used for both problems. The relevant operators need to be assembled only once in each iteration step and the evaluation of the domain derivative becomes very efficient when fast solvers for the discrete equations are available.

In section 2 we start by providing mathematical preliminaries and formulating both the direct and the inverse scattering problems for general scatterers. We also describe the principal approach of solving an inverse scattering problem by a reconstruction algorithm of Gauss–Newton type that minimizes the residual in a non-linear ill-posed operator equation for the far field map. We recall the characterization of domain derivatives of this map via boundary value problems. In section 3, we define the long tubular obstacles of interest and consider perturbations of their surfaces. Our main theoretical results are Theorem 3.5 in which we characterize the domain derivative of the far field map for such specific obstacles and Corollary 3.7 which gives explicit expressions of the linearizations. Based on the boundary value problem formulation discussed in section 2, both results combined provide computable expressions for the domain derivative that can be used in the concrete implementation of an iterative reconstruction algorithm. Such an implementation is discussed in section 4. Suitable regularization terms for the objective functional are introduced. The boundary value problems can be solved using boundary integral equations. We conclude by providing three examples of reconstructions of scatterers in different configurations.

2 The inverse electromagnetic scattering problem

In this section we give an overview over the mathematical formulation of both the direct and the inverse scattering problem. Before we do so, we first introduce some differential operators together with some spaces and traces that are required for the study of time-harmonic Maxwell's equations.

The differential operators **grad**, div, **curl** and Δ denote the variational (or weak) gradient, divergence, rotation and Laplace operator, respectively. We use the standard Sobolev spaces $H^1(D')$, $H^1(D', \mathbb{C}^3)$ as well as

$$H(\mathbf{curl}^p, D') \;=\; \left\{ \boldsymbol{u} \in L^2(D') \,:\; \mathbf{curl}^j \boldsymbol{u} \in L^2(D', \mathbb{C}^3)\,, \quad j = 1, \ldots, p \right\},$$

which are defined for any Lipschitz domain $D' \subseteq \mathbb{R}^3$. As usual, an index "loc" denotes spaces of functions that are in the corresponding Sobolev space for every compact subdomain. The trace spaces $H^s(\partial D')$, $H^s(\partial D', \mathbb{C}^3)$, $s = \pm 1/2$ are also standard. For $\boldsymbol{U} \in H^1(D', \mathbb{C}^3)$, we also define the tangential trace $\gamma_t \boldsymbol{U} = \boldsymbol{U} \times \boldsymbol{\nu}$ on $\partial D'$ and the corresponding boundary space $V_t = \gamma_t(H^1(D', \mathbb{C}^3))$. The dual space V_t^* is defined via an extension of the bilinear form

$$\langle \boldsymbol{U}\,,\, \boldsymbol{V} \rangle_{t, \partial D'} \;=\; \int_{\partial D'} \boldsymbol{U} \cdot (\boldsymbol{\nu} \times \boldsymbol{V})\, \mathrm{d}s\,, \qquad \boldsymbol{U},\, \boldsymbol{V} \in L_t^2(\partial D')\,,$$

where $L_t^2(\partial D')$ denotes the space of square integrable tangential vector fields on $\partial D'$. Also, the surface divergence operator Div on $\partial D'$ may be defined for distributions in V_t^* by a suitable extension (see [2] for details). The tangential trace γ_t can be extended to a bounded, surjective operator $\gamma_t : H(\mathbf{curl}, D') \to H^{-1/2}(\mathrm{Div}, \partial D')$, where

$$H^{-1/2}(\mathrm{Div}, \partial D') \;=\; \left\{ \boldsymbol{V} \in V_t^* \,:\, \mathrm{Div}\, \boldsymbol{V} \in H^{-1/2}(\partial D') \right\}.$$

Let $\eta : H^{1/2}(\partial D') \to H^1(D')$ denote a bounded right inverse of the Dirichlet trace $\gamma_0 : H^1(D') \to H^{1/2}(\partial D')$. The vectorial surface curl operator $\mathbf{Curl} = \gamma_t \,\mathbf{grad}\, \eta : H^{1/2}(\partial D') \to H^{-1/2}(\mathrm{Div}, \partial D')$ is bounded. Additionally, we introduce the Neumann trace $\gamma_N \colon H(\mathbf{curl}^2, D') \to H^{-1/2}(\mathrm{Div}, \partial D')$,

$$\gamma_N \boldsymbol{U} \;=\; \frac{1}{\mathrm{i}\omega\mu}\, \gamma_t\, \mathbf{curl}\, \boldsymbol{U}\,, \qquad \boldsymbol{U} \in H(\mathbf{curl}^2, D')\,.$$

Denote by ω the angular frequency, by ε_0 and μ_0 the electric permittivity and magnetic permeability of the homogeneous background medium and by $k = \omega\sqrt{\varepsilon_0 \mu_0}$ the wave number. In our scattering problem, let the pair $(\boldsymbol{E}^i, \boldsymbol{H}^i)$ denote smooth incident fields that satisfy the time-harmonic Maxwell's equations

$$\mathbf{curl}\, \boldsymbol{E}^i - \mathrm{i}\omega\mu_0\, \boldsymbol{H}^i \;=\; 0\,, \quad \mathbf{curl}\, \boldsymbol{H}^i + \mathrm{i}\omega\varepsilon_0\, \boldsymbol{E}^i \;=\; 0 \qquad \text{in } \mathbb{R}^3\,. \tag{1}$$

We assume the scattering object to be a bounded tubular C^1-smooth domain $D \subseteq \mathbb{R}^3$ such that $\mathbb{R}^3 \setminus \overline{D}$ is connected. Throughout this work, the exterior unit normal to ∂D is denoted by $\boldsymbol{\nu}$. Even though we study Maxwell's equations for these scattering objects, we note that many of the results reported here hold in the more general case of a Lipschitz domain. We assume that incident fields $\boldsymbol{E}^i$, $\boldsymbol{H}^i$ satisfying (1) illuminate the scatterer D. The interaction of the incident fields with the medium D produces scattered fields $\boldsymbol{E}^s$, $\boldsymbol{H}^s$, which constitute a solution to the time-harmonic Maxwell's equations away from the scatterer and which satisfy the Silver–Müller radiation condition

$$\lim_{|\boldsymbol{x}| \to \infty} |\boldsymbol{x}|\, (\sqrt{\mu_0}\, \boldsymbol{H}^s(\boldsymbol{x}) \times \widehat{\boldsymbol{x}} - \sqrt{\varepsilon_0}\, \boldsymbol{E}^s(\boldsymbol{x})) \;=\; 0 \tag{2}$$

uniformly with respect to the direction of observation $\widehat{\boldsymbol{x}} := \boldsymbol{x}/|\boldsymbol{x}| \in \mathbb{S}^2 := \{\boldsymbol{y} \in \mathbb{R}^3 : |\boldsymbol{y}| = 1\}$. A pair of fields satisfying (2) is called radiating. We distinguish between two different models for the

scattering object D, which result in contrasting boundary conditions on ∂D for the scattered fields. The first model is the perfect conductor model. The scattering problem is to determine the vector fields $\boldsymbol{E}^s$, $\boldsymbol{H}^s \in H_{\mathrm{loc}}(\mathbf{curl}, \mathbb{R}^3 \setminus \overline{D})$ that satisfy

$$\mathbf{curl}\, \boldsymbol{E}^s - \mathrm{i}\omega\mu_0\, \boldsymbol{H}^s = 0\,, \quad \mathbf{curl}\, \boldsymbol{H}^s + \mathrm{i}\omega\varepsilon_0\, \boldsymbol{E}^s = 0 \qquad \text{in } \mathbb{R}^3 \setminus \overline{D}\,, \tag{3a}$$

$$\gamma_t \boldsymbol{E}^s = -\gamma_t \boldsymbol{E}^i \qquad \text{on } \partial D \tag{3b}$$

together with the Silver–Müller radiation condition (2). The second model describes a penetrable scattering object. In this case we introduce piecewise constant permittivity and permeability distributions ε and μ with $\varepsilon = \varepsilon_1$, $\mu = \mu_1$ in D and $\varepsilon = \varepsilon_0$, $\mu = \mu_0$ in $\mathbb{R}^3 \setminus \overline{D}$. The Maxwell system for this transmission problem is to find the vector fields $\boldsymbol{E}^s$, $\boldsymbol{H}^s \in H_{\mathrm{loc}}(\mathbf{curl}, \mathbb{R}^3 \setminus \overline{D}) \cup H(\mathbf{curl}, D)$ that fulfill

$$\begin{aligned} \mathbf{curl}\, \boldsymbol{E}^s - \mathrm{i}\omega\mu_0\, \boldsymbol{H}^s = 0\,, \quad \mathbf{curl}\, \boldsymbol{H}^s + \mathrm{i}\omega\varepsilon_0\, \boldsymbol{E}^s = 0 \qquad & \text{in } \mathbb{R}^3 \setminus \overline{D}\,, \\ \mathbf{curl}\, \boldsymbol{E}^s - \mathrm{i}\omega\mu_1\, \boldsymbol{H}^s = 0\,, \quad \mathbf{curl}\, \boldsymbol{H}^s + \mathrm{i}\omega\varepsilon_1\, \boldsymbol{E}^s = 0 \qquad & \text{in } D\,, \end{aligned} \tag{4a}$$

$$[\gamma_t \boldsymbol{E}^s]_{\partial D} = -\gamma_t \boldsymbol{E}^i\,, \qquad [\gamma_t \boldsymbol{H}^s]_{\partial D} = -\gamma_t \boldsymbol{H}^i \qquad \text{on } \partial D \tag{4b}$$

together with the Silver–Müller radiation condition (2). Here, $[\,\cdot\,]_{\partial D}$ denotes the difference of the boundary values taken from outside and inside of D, respectively. It is well-known that under our assumptions, both of these problems are uniquely solvable (see, e.g., [18, Ch. 10, 11]).

As a consequence of (2), for both problems (3) and (4), the scattered electric field $\boldsymbol{E}^s$ can be asymptotically expanded as

$$\boldsymbol{E}^s(\boldsymbol{x}) = \frac{\mathrm{e}^{\mathrm{i}k|\boldsymbol{x}|}}{4\pi|\boldsymbol{x}|}\big(\boldsymbol{E}^\infty(\widehat{\boldsymbol{x}}) + \mathrm{O}\big(|\boldsymbol{x}|^{-1}\big)\big)\,, \qquad |\boldsymbol{x}| \to \infty\,,$$

uniformly with respect to $\widehat{\boldsymbol{x}} = \boldsymbol{x}/|\boldsymbol{x}|$. The density $\boldsymbol{E}^\infty \in L_t^2(\mathbb{S}^2)$ is called the electric far field pattern.

We address the inverse problem to reconstruct the boundary ∂D of the tubular scattering object D from knowledge of $\boldsymbol{E}^\infty$ for one single pair of incident fields $\boldsymbol{E}^i$, $\boldsymbol{H}^i$. It is not known whether this problem possesses a unique solution. However, promising numerical reconstructions have been reported for star-shaped obstacles using iterative methods based on the shape derivative of the far field pattern [12]. This is the approach that we also use in the present paper. In the remainder of this section we give a brief summary of results concerning shape-derivatives for electromagnetic scattering problems based on domain derivatives (see [12–14] for details). Formally, we consider the map

$$F : \mathcal{M} \to L_t^2(\mathbb{S}^2)\,, \quad \partial D \mapsto \boldsymbol{E}^\infty\,, \tag{5}$$

that maps boundaries of scattering objects ∂D from an admissible set $\mathcal{M}$ to the electric far field pattern that is generated upon illumination of D with $\boldsymbol{E}^i$, $\boldsymbol{H}^i$. We refer to this map as the far field map.

To establish the linearization of the far field map with respect to boundary variations, consider a sufficiently small $\boldsymbol{\eta} \in C^1(\mathbb{R}^3, \mathbb{R}^3)$, compactly supported in a neighborhood of ∂D such that the map $\boldsymbol{x} \mapsto \boldsymbol{x} + \boldsymbol{\eta}(\boldsymbol{x})$ is a diffeomorphism and maps D to a perturbed domain $D_{\boldsymbol{\eta}}$ with boundary $\partial D_{\boldsymbol{\eta}} = \{\boldsymbol{y} = \boldsymbol{x} + \boldsymbol{\eta}(\boldsymbol{x}) : \boldsymbol{x} \in \partial D\}$. For such perturbations of D it has been shown that there exists the domain derivative $\boldsymbol{E}'$ of the scattered field [14], a radiating solution of Maxwell's equations with far field $\boldsymbol{E}'^\infty = F'[\partial D]\boldsymbol{\eta}$ depending linearly on $\boldsymbol{\eta}$, such that

$$\frac{1}{\|\boldsymbol{\eta}\|_{1,\infty}} \|F(\partial D_{\boldsymbol{\eta}}) - F(\partial D) - F'[\partial D]\boldsymbol{\eta}\|_{L_t^2(\mathbb{S}^2)} \to 0\,, \qquad \|\boldsymbol{\eta}\|_{1,\infty} \to 0\,. \tag{6}$$

In the perfect conductor case (3), the fields $\boldsymbol{E}'$, $\boldsymbol{H}' \in H_{\mathrm{loc}}(\mathbf{curl}, \mathbb{R}^3 \setminus \overline{D})$ are radiating solutions of (3a) with the boundary condition (3b) replaced by

$$\gamma_t \boldsymbol{E}' \;=\; \mathrm{i}\omega\mu_0\, \boldsymbol{\eta}_{\boldsymbol{\nu}}\, \boldsymbol{\nu} \times \gamma_N \boldsymbol{E} - \mathbf{Curl}(\boldsymbol{\eta}_{\boldsymbol{\nu}} \boldsymbol{E}_{\boldsymbol{\nu}}) \qquad \text{on } \partial D\,, \tag{7}$$

see [13,19]. Here $\boldsymbol{E} = \boldsymbol{E}^i + \boldsymbol{E}^s$ is the total electric field of the original scattering problem (3) and the index $\boldsymbol{\nu}$ denotes the normal component of the corresponding vector fields. For penetrable media the situation is similar [14]: The fields $\boldsymbol{E}'$, $\boldsymbol{H}' \in H_{\mathrm{loc}}(\mathbf{curl}, \mathbb{R}^3 \setminus \overline{D}) \cup H(\mathbf{curl}, D)$ are radiating solutions of (4a) with the transmission condition (4b) replaced by

$$\begin{aligned} [\gamma_t \boldsymbol{E}']_{\partial D} \;&=\; \mathrm{i}\omega\, [\mu]_{\partial D}\, \boldsymbol{\eta}_{\boldsymbol{\nu}}\, (\boldsymbol{\nu} \times \gamma_t \boldsymbol{H}) - [\mathbf{Curl}(\boldsymbol{\eta}_{\boldsymbol{\nu}} \boldsymbol{E}_{\boldsymbol{\nu}})]_{\partial D} \\ [\gamma_t \boldsymbol{H}']_{\partial D} \;&=\; -\mathrm{i}\omega\, [\varepsilon]_{\partial D}\, \boldsymbol{\eta}_{\boldsymbol{\nu}}\, (\boldsymbol{\nu} \times \gamma_t \boldsymbol{E}) - [\mathbf{Curl}(\boldsymbol{\eta}_{\boldsymbol{\nu}} \boldsymbol{H}_{\boldsymbol{\nu}})]_{\partial D} \end{aligned} \qquad \text{on } \partial D\,, \tag{8}$$

where now $\boldsymbol{E} = \boldsymbol{E}^i + \boldsymbol{E}^s$, $\boldsymbol{H} = \boldsymbol{H}^i + \boldsymbol{H}^s$ are the total fields in the original problem (4).

One usually assumes that ∂D is represented by an element of some metric space $\mathcal{M}$. In much of the literature on iterative methods for inverse scattering problems, only star shaped obstacles are considered. Then $\mathcal{M}$ is the set of positive functions on the unit sphere representing the distance of each point on ∂D from the origin. In this paper, we consider tubular scatterers and $\mathcal{M}$ is a set of admissible parametrizations of objects of this type. Exact definitions are given in section 3 below. In a slight abuse of notation, we henceforth consider $F : \mathcal{M} \to L_t^2(\mathbb{S}^2)$, $X \mapsto \boldsymbol{E}^\infty$, where ∂D is represented by X. Thus, either inverse problem can be formulated as: Given $\boldsymbol{E}^\infty_{\mathrm{data}} \in L_t^2(\mathbb{S}^2)$, find $X \in \mathcal{M}$ such that

$$F(X) \;=\; \boldsymbol{E}^\infty_{\mathrm{data}}\,. \tag{9}$$

Linearizing (9) leads to the Gauss–Newton iteration

$$X_{n+1} \;=\; X_n + H_n\,, \qquad F'[X_n] H_n \;=\; \boldsymbol{E}^\infty_{\mathrm{data}} - F(X_n)\,.$$

We note that in this formulation we automatically avoid the difficulty that for a boundary surface ∂D with representation $X \in \mathcal{M}$, the perturbed domain $\partial D_{\boldsymbol{\eta}}$ may not have such a representation. By directly perturbing X, we stay inside the admissible class of domains.

3 Tubular obstacles

The obstacles that we discuss in this work are longitudinal objects that follow a central spine curve C. The cross section that is perpendicular to the center curve is assumed to be a disc at each point, but the radius r may vary along the curve.

Let us start by reminding the reader of some results concerning perturbations of regular curves obtained in [11]. Let $\boldsymbol{z} : [0,1] \to \mathbb{R}^3$ be a parametrization of a C^2-smooth regular curve C. By $(\boldsymbol{t}, \boldsymbol{n}, \boldsymbol{b})$ we denote a continuous orthogonal frame accompanying C, i.e., at every $\tau \in [0,1]$, we have $\boldsymbol{t}(\tau) = \boldsymbol{z}'(\tau)/|\boldsymbol{z}'(\tau)|$ and $(\boldsymbol{t}(\tau), \boldsymbol{n}(\tau), \boldsymbol{b}(\tau))$ is an orthonormal basis of $\mathbb{R}^3$. Moreover, all three vectors continuously depend on τ. Let $\boldsymbol{\delta} : [0,1] \to \mathbb{R}^3$ denote the parametrization of another C^2-curve. Then, [11, Proof of Lem. 4.1] yields a continuous orthogonal frame of the curve parametrized by $\boldsymbol{z} + \boldsymbol{\delta}$ denoted by $(\boldsymbol{t}_{\boldsymbol{\delta}}, \boldsymbol{n}_{\boldsymbol{\delta}}, \boldsymbol{b}_{\boldsymbol{\delta}})$ given by

$$\begin{aligned} \boldsymbol{t}_{\boldsymbol{\delta}} \;&=\; \frac{\boldsymbol{z}' + \boldsymbol{\delta}'}{|\boldsymbol{z}' + \boldsymbol{\delta}'|}\,, \\ \boldsymbol{n}_{\boldsymbol{\delta}} \;&=\; (\boldsymbol{t} \cdot \boldsymbol{t}_{\boldsymbol{\delta}})\, \boldsymbol{n} - \frac{\boldsymbol{b} \cdot \boldsymbol{t}_{\boldsymbol{\delta}}}{1 + \boldsymbol{t} \cdot \boldsymbol{t}_{\boldsymbol{\delta}}}\, (\boldsymbol{t} \times \boldsymbol{t}_{\boldsymbol{\delta}}) - (\boldsymbol{n} \cdot \boldsymbol{t}_{\boldsymbol{\delta}})\, \boldsymbol{t}\,, \\ \boldsymbol{b}_{\boldsymbol{\delta}} \;&=\; (\boldsymbol{t} \cdot \boldsymbol{t}_{\boldsymbol{\delta}})\, \boldsymbol{b} + \frac{\boldsymbol{n} \cdot \boldsymbol{t}_{\boldsymbol{\delta}}}{1 + \boldsymbol{t} \cdot \boldsymbol{t}_{\boldsymbol{\delta}}}\, (\boldsymbol{t} \times \boldsymbol{t}_{\boldsymbol{\delta}}) - (\boldsymbol{b} \cdot \boldsymbol{t}_{\boldsymbol{\delta}})\, \boldsymbol{t}\,. \end{aligned}$$

Moreover, an asymptotic expansion with respect to the magnitude of the perturbation is provided, which reads

$$\boldsymbol{t}_{\boldsymbol{\delta}} \;=\; \boldsymbol{t} + \frac{\boldsymbol{\delta}'}{|\boldsymbol{z}'|} - \frac{\boldsymbol{\delta}' \cdot \boldsymbol{t}}{|\boldsymbol{z}'|}\,\boldsymbol{t} + \mathrm{o}\left(\|\boldsymbol{\delta}'\|_\infty\right), \tag{11a}$$

$$\boldsymbol{n}_{\boldsymbol{\delta}} \;=\; \boldsymbol{n} - \frac{\boldsymbol{\delta}' \cdot \boldsymbol{n}}{|\boldsymbol{z}'|}\,\boldsymbol{t} + \mathrm{o}\left(\|\boldsymbol{\delta}'\|_\infty\right), \tag{11b}$$

$$\boldsymbol{b}_{\boldsymbol{\delta}} \;=\; \boldsymbol{b} - \frac{\boldsymbol{\delta}' \cdot \boldsymbol{b}}{|\boldsymbol{z}'|}\,\boldsymbol{t} + \mathrm{o}\left(\|\boldsymbol{\delta}'\|_\infty\right) \tag{11c}$$

as $\|\boldsymbol{\delta}'\|_\infty \to 0$. We note that the condition that $(\boldsymbol{t}, \boldsymbol{n}, \boldsymbol{b})$ is continuous on $[0,1]$ will not necessarily be satisfied by the Frénet frame, which is the standard accompanying orthogonal frame used in differential geometry. If the curvature of C vanishes at some point, the Frénet frame is not defined in that point, and a continuous extension may also not be possible. In the worst case of a straight line the Frénet frame is not defined for any point. Instead, we use rotation minimizing frames known, e.g., from applications in computer graphics [21].

Definition 3.1 *Let $\boldsymbol{z} : [0,1] \to \mathbb{R}^3$ be a parametrization of a C^2-smooth regular curve C. The frame $(\boldsymbol{t}, \boldsymbol{n}, \boldsymbol{b}) \in C^1([0,1], \mathbb{R}^{3\times 3})$ is called a rotation minimizing frame of C, if*

$$\boldsymbol{t} \;=\; \frac{\boldsymbol{z}'}{|\boldsymbol{z}'|}, \qquad \boldsymbol{t} \cdot \boldsymbol{n} \;=\; 0\,, \qquad \boldsymbol{n}' \;=\; -(\boldsymbol{t}' \cdot \boldsymbol{n})\,\boldsymbol{t}\,, \qquad \boldsymbol{b} \;=\; \boldsymbol{t} \times \boldsymbol{n} \qquad \text{on} \quad [0,1]\,.$$

Given a curve C with a rotation minimizing frame, we now turn to the definition of the surface of a long tubular obstacle having C as its spine curve. Such a surface will be represented by an atlas of three charts, $\boldsymbol{x}_{\mathrm{body}}$, $\boldsymbol{x}_{\mathrm{start}}$ and $\boldsymbol{x}_{\mathrm{end}}$, parametrizing the tubular body S_{body}, the start cap S_{start} and the end cap S_{end}, respectively. To define these charts, we additionally introduce the vectors

$$\boldsymbol{\zeta}(\tau, \varphi) \;=\; \cos(\varphi)\,\boldsymbol{n}(\tau) + \sin(\varphi)\,\boldsymbol{b}(\tau)\,, \tag{12a}$$

$$\boldsymbol{\xi}_{\mathrm{start}}(\vartheta, \varphi) \;=\; \cos(\varphi)\,\sin(\vartheta)\,\boldsymbol{b}(0) + \sin(\varphi)\sin(\vartheta)\,\boldsymbol{n}(0) - \cos(\vartheta)\,\boldsymbol{t}(0)\,, \tag{12b}$$

$$\boldsymbol{\xi}_{\mathrm{end}}(\vartheta, \varphi) \;=\; \cos(\varphi)\,\sin(\vartheta)\,\boldsymbol{n}(1) + \sin(\varphi)\sin(\vartheta)\,\boldsymbol{b}(1) + \cos(\vartheta)\,\boldsymbol{t}(1)\,, \tag{12c}$$

where $\tau \in [0,1]$, $\varphi \in (-\pi, \pi]$ and $\vartheta \in [0, \pi/2]$. The charts are given by

$$\boldsymbol{x}_{\mathrm{body}}(\tau, \varphi) \;=\; \boldsymbol{z}(\tau) + r(\tau)\,\boldsymbol{\zeta}(\tau, \varphi)\,, \tag{13a}$$

$$\boldsymbol{x}_{\mathrm{start}}(\vartheta, \varphi) \;=\; \boldsymbol{z}(0) + \rho_0(\vartheta, \varphi)\,\boldsymbol{\xi}_{\mathrm{start}}(\vartheta, \varphi) \tag{13b}$$

$$\boldsymbol{x}_{\mathrm{end}}(\vartheta, \varphi) \;=\; \boldsymbol{z}(1) + \rho_1(\vartheta, \varphi)\,\boldsymbol{\xi}_{\mathrm{end}}(\vartheta, \varphi) \tag{13c}$$

where $\tau \in [0,1]$, $\varphi \in (-\pi, \pi]$ and $\vartheta \in [0, \pi/2]$ (see Figure 1 for an illustration). The functions ρ_0 and ρ_1 need to be chosen in such a way that the resulting surface is C^1-smooth. To achieve this, we establish some helpful results.

Lemma 3.2 *Let $\boldsymbol{z} : [0,1] \to \mathbb{R}^3$ a parametrization of a C^2-smooth regular curve C and $(\boldsymbol{t}, \boldsymbol{n}, \boldsymbol{b}) \in C^1([0,1], \mathbb{R}^{3\times 3})$ a rotation minimizing frame of C. Then*

$$\partial_\tau \boldsymbol{x}_{\mathrm{body}} \;=\; \psi\,\boldsymbol{t} + r'\,\boldsymbol{\zeta} \qquad \text{with} \qquad \psi \;=\; |\boldsymbol{z}'| - r\,\boldsymbol{t}' \cdot \boldsymbol{\zeta}\,. \tag{14}$$

Proof: From Definition 3.1, we have

$$\boldsymbol{b}' \;=\; \boldsymbol{t}' \times \boldsymbol{n} - (\boldsymbol{t}' \cdot \boldsymbol{n})\,(\boldsymbol{t} \times \boldsymbol{t}) \;=\; \boldsymbol{t}' \times (\boldsymbol{b} \times \boldsymbol{t}) \;=\; (\boldsymbol{t}' \cdot \boldsymbol{t})\,\boldsymbol{b} - (\boldsymbol{t}' \cdot \boldsymbol{b})\,\boldsymbol{t}\,.$$

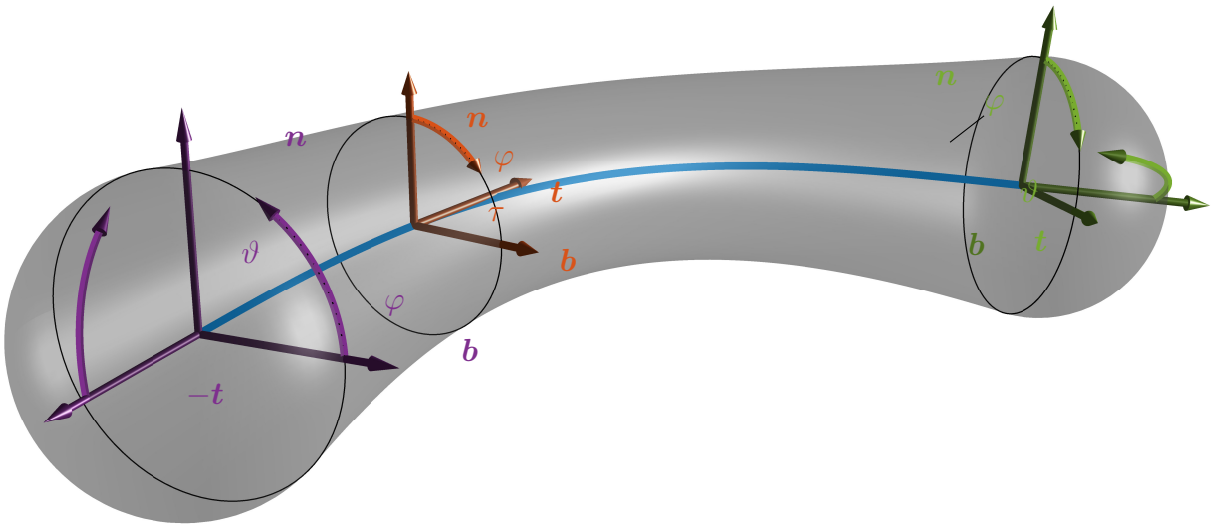

Figure 1: Parameters used for the parametrizations $\boldsymbol{x}_{\text{start}}$ (purple), $\boldsymbol{x}_{\text{body}}$ (orange) and $\boldsymbol{x}_{\text{end}}$ (green) of the tube surface together with the underlying coordinate systems.

As $|\boldsymbol{t}| = 1$, there holds $\boldsymbol{t}' \cdot \boldsymbol{t} = 0$ and hence $\boldsymbol{b}' = -(\boldsymbol{t}' \cdot \boldsymbol{b})\,\boldsymbol{t}$. Thus, $\partial_\tau \boldsymbol{\zeta}(\tau, \varphi) = -(\boldsymbol{t}' \cdot \boldsymbol{\zeta})\,\boldsymbol{t}$ follows. As $\boldsymbol{z}' = |\boldsymbol{z}'|\,\boldsymbol{t}$, the assertion follows from the product rule. ∎

It is straightforward to obtain that

$$\boldsymbol{t}' \;=\; \frac{\boldsymbol{z}''}{|\boldsymbol{z}'|} - \left(\frac{\boldsymbol{z}''}{|\boldsymbol{z}'|} \cdot \boldsymbol{t}\right) \boldsymbol{t}\,.$$

We now assume $\|r\|_\infty$ to be small enough such that $\psi \geq c > 0$ and set

$$\rho_\tau(\vartheta, \varphi) \;=\; r(\tau) - \eta_\tau(\vartheta, \varphi)\,, \quad \tau \in \{0\,, 1\}\,, \tag{15}$$

with

$$\eta_0(\vartheta, \varphi) \;=\; \frac{4\vartheta^2\,(\vartheta - \frac{\pi}{2})\,r(0)\,r'(0)}{\pi^2\,\psi\left(0, \frac{\pi}{2} - \varphi\right)}\,, \qquad \eta_1(\vartheta, \varphi) \;=\; \frac{4\vartheta^2\,(\vartheta - \frac{\pi}{2})\,r(1)\,r'(1)}{\pi^2\,\psi\,(1, \varphi)}\,.$$

The following Lemma is proven in Appendix A as the proof just consists of straightforward technical calculations.

Lemma 3.3 *Let $\boldsymbol{z} : [0,1] \to \mathbb{R}^3$ be a parametrization of a C^2-smooth regular curve C and let $(\boldsymbol{t}, \boldsymbol{n}, \boldsymbol{b}) \in C^1([0,1], \mathbb{R}^{3\times 3})$ be a rotation minimizing frame of C. If $\|r\|_{2,\infty}$ is sufficiently small, then $\boldsymbol{x}_{\text{body}}$, $\boldsymbol{x}_{\text{start}}$ and $\boldsymbol{x}_{\text{end}}$ given by (13) and (15) are the atlas of a C^1-smooth surface.*

In the setting of the previous section, each obstacle D is, thus, represented by an element $X = (\boldsymbol{z}, r)$ of the set

$$\mathcal{M} = \left\{(\widehat{\boldsymbol{z}}, \widehat{r}) :\; \widehat{\boldsymbol{z}} : [0,1] \to \mathbb{R}^3 \; C^2\text{-smooth, regular and } \widehat{r} \in C^1([0,1]),\; \widehat{r} > 0\right\}. \tag{16}$$

We note that not every element of $\mathcal{M}$ yields an atlas of a regular C^1-surface. Restrictions on the curvature of $\boldsymbol{z}$ and the magnitude of r apply.

We proceed by formulating a theorem that characterizes the domain derivative of the electromagnetic far field map for tubular obstacles, both in the case of a perfectly conducting and a penetrable obstacle. We vary the shape of the obstacle represented by $(\boldsymbol{z}, r) \in \mathcal{M}$ by considering $(\boldsymbol{z} + \boldsymbol{\delta}, r + \varepsilon) \in \mathcal{M}$ for $(\boldsymbol{\delta}, \varepsilon)$ sufficiently small in norm. In what follows, quantities, which are perturbed in this way are equipped with an additional index $(\boldsymbol{\delta}, \varepsilon)$.

Lemma 3.4 *Let ∂D denote a regular C^1-surface represented by $(\boldsymbol{z}, r) \in \mathcal{M}$. The function defined on ∂D by*

$$\boldsymbol{h}_{(\boldsymbol{\delta},\varepsilon)}(\boldsymbol{x}) \;=\; \boldsymbol{x}_{\ell,(\boldsymbol{\delta},\varepsilon)}(\boldsymbol{x}_\ell^{-1}(\boldsymbol{x})) - \boldsymbol{x}\,, \qquad \boldsymbol{x} \in S_\ell\,, \quad \ell \in \{\text{body},\ \text{start},\ \text{end}\}\,, \tag{17}$$

for sufficiently small $\|(\boldsymbol{\delta},\varepsilon)\|_{2,\infty\times 1,\infty}$ is C^1-smooth on ∂D and depends smoothly on the quantities $\boldsymbol{\delta}, \boldsymbol{\delta}', \boldsymbol{\delta}'', \varepsilon, \varepsilon'$ in $C^1(\partial D)$.

Proof: From (13) it is clear that in the neighborhood of almost every point on ∂D, with the exceptions of the points $\boldsymbol{z}(0) - r(0)\,\boldsymbol{t}(0)$, $\boldsymbol{z}(1) + r(1)\,\boldsymbol{t}(1)$ on the caps, the charts are diffeomorphisms. Then, for sufficiently small $\|(\boldsymbol{\delta},\varepsilon)\|_{2,\infty\times 1,\infty}$, by definition, $\boldsymbol{h}_{(\boldsymbol{\delta},\varepsilon)}$ is C^1-smooth except at these isolated points. In a neighborhood of these points, we may instead use a regular parameterization of the surface, for example by projection on the tangential plane, to extend the definition.

An inspection of the asymptotic formulas in (11) together with (12) and (13) reveals that $\boldsymbol{x}_{\text{body}}$ depends smoothly on $\boldsymbol{\delta}$, $\boldsymbol{\delta}'$ and ε, while $\boldsymbol{x}_{\text{start}}$ and $\boldsymbol{x}_{\text{end}}$ also depend on $\boldsymbol{\delta}''(0)$, $\varepsilon'(0)$ and $\boldsymbol{\delta}''(1)$, $\varepsilon'(1)$, respectively. Straightforward calculations then yield that all three charts and their inverses smoothly depend on $\boldsymbol{\delta}$, $\boldsymbol{\delta}'$, $\boldsymbol{\delta}''$, ε, ε'. The same is consequently true for $\boldsymbol{h}_{(\boldsymbol{\delta},\varepsilon)}$. ∎

The next theorem characterizes the electromagnetic domain derivative for tubular objects D with boundary ∂D parametrized as in (13). The linearization of $\boldsymbol{h}_{(\boldsymbol{\delta},\varepsilon)}$ with respect to the perturbation $(\boldsymbol{\delta},\varepsilon)$, denoted by $\boldsymbol{h} \in C^1(\partial D)$, plays an essential role here. As the theorem and its proof show, both terms $F'[\partial D]\boldsymbol{h}_{(\boldsymbol{\delta},\varepsilon)}$ and $F'[\partial D]\boldsymbol{h}$ satisfying (6) exist and fulfill

$$F'[\partial D]\boldsymbol{h}_{(\boldsymbol{\delta},\varepsilon)} \;=\; F'[\partial D]\boldsymbol{h} + \mathrm{o}(\|\boldsymbol{\delta}\|_{2,\infty} + \|\varepsilon\|_{1,\infty}) \qquad \text{as } \|\boldsymbol{\delta}\|_{2,\infty}\,,\ \|\varepsilon\|_{1,\infty} \to 0\,.$$

Thus, instead of dealing with $\boldsymbol{h}_{(\boldsymbol{\delta},\varepsilon)}$, which involves the inverse of the parametrization in ∂D from (13), one can consider only its linearization $\boldsymbol{h}$, which is significantly easier to compute and implement numerically.

Theorem 3.5 *Let ∂D denote a regular C^1-surface represented by $(\boldsymbol{z}, r) \in \mathcal{M}$. Let $\boldsymbol{h} \in C^1(\partial D)$ denote the linearization of $\boldsymbol{h}_{(\boldsymbol{\delta},\varepsilon)}$ with respect to $(\boldsymbol{\delta},\varepsilon)$, so that*

$$\lim_{\|\boldsymbol{\delta}\|_{2,\infty},\|\varepsilon\|_{1,\infty}\to 0} \frac{\|\boldsymbol{h}_{(\boldsymbol{\delta},\varepsilon)} - \boldsymbol{h}\|_{1,\infty}}{\|\boldsymbol{\delta}\|_{2,\infty} + \|\varepsilon\|_{1,\infty}} \;=\; 0\,. \tag{18}$$

The far field map F from (5) with $\mathcal{M}$ as in (16) is Fréchet differentiable at $(\boldsymbol{z}, r)$. With the linearization $\boldsymbol{h}$ as given above, the Fréchet derivative $F'[\partial D]\boldsymbol{h}$ from (6), represented via $F'[\boldsymbol{z}, r](\boldsymbol{\delta},\varepsilon)$, satisfies $F'[\partial D](\boldsymbol{\delta},\varepsilon) = \boldsymbol{E}'^{\infty}$. Here, $\boldsymbol{E}'$ is the unique solution of (3a) together with (7) in the case of a perfect conducting obstacle and of (4a) together with (8) in the case of a penetrable obstacle, where in both cases (7) and (8), the perturbation $\boldsymbol{\eta}$ is replaced by $\boldsymbol{h}$.

The proof of Theorem 3.5 requires the explicit computation of the linearization $\boldsymbol{h}$ for given $\boldsymbol{h}_{(\boldsymbol{\delta},\varepsilon)}$. In the following lemma, we start its derivation by studying the asymptotic behavior of the quantities involved in the surface parametrizations with respect to $\boldsymbol{\delta}$ and ε. As these results are purely technical in nature, we formulate them in a separate lemma that we prove in Appendix B.

Lemma 3.6 *It holds that*

$$\psi_{(\boldsymbol{\delta},\varepsilon)} \;=\; \psi - (\boldsymbol{t}' \cdot \boldsymbol{\zeta})\,\varepsilon + \boldsymbol{\delta}' \cdot \boldsymbol{t} - r\left(\frac{1}{|\boldsymbol{z}'|}\,\boldsymbol{\delta}'' - \frac{\boldsymbol{\delta}' \cdot \boldsymbol{t}}{|\boldsymbol{z}'|^2}\,\boldsymbol{z}'' - \frac{\boldsymbol{z}'' \cdot \boldsymbol{t}}{|\boldsymbol{z}'|^2}\,\boldsymbol{\delta}'\right) \cdot \boldsymbol{\zeta} + \mathrm{o}\left(\|\boldsymbol{\delta}\|_{2,\infty} + \|\varepsilon\|_{\infty}\right)$$

as $\|\boldsymbol{\delta}\|_{2,\infty}$, $\|\varepsilon\|_{\infty} \to 0$, as well as

$$\rho_{\tau,(\boldsymbol{\delta},\varepsilon)} \;=\; \rho_\tau + \sum_{j=0}^{1} \mu_{j,\tau}\,\varepsilon^{(j)}(\tau) + \sum_{j=1}^{2} \boldsymbol{\nu}_{j,\tau} \cdot \boldsymbol{\delta}^{(j)}(\tau) + \mathrm{o}\left(\|\boldsymbol{\delta}\|_{2,\infty} + \|\varepsilon\|_{1,\infty}\right), \quad \tau \in \{0\,, 1\}\,,$$

as $\|\boldsymbol{\delta}\|_{2,\infty},\ \|\varepsilon\|_{1,\infty} \to 0$, *where*

$$\begin{aligned}
\mu_{0,0}(\vartheta,\varphi) &= 1 - \frac{\eta_0(\vartheta,\varphi)}{r(0)} - \frac{\eta_0(\vartheta,\varphi)}{\psi(0,\frac{\pi}{2}-\varphi)}\,\boldsymbol{t}'(0)\cdot\boldsymbol{\zeta}(0,\varphi)\,, & \mu_{1,0}(\vartheta,\varphi) &= -\frac{\eta_0(\vartheta,\varphi)}{r'(0)}\,,\\
\mu_{0,1}(\vartheta,\varphi) &= 1 - \frac{\eta_1(\vartheta,\varphi)}{r(1)} - \frac{\eta_1(\vartheta,\varphi)}{\psi(1,\varphi)}\,\boldsymbol{t}'(1)\cdot\boldsymbol{\zeta}(1,\varphi)\,, & \mu_{1,1}(\vartheta,\varphi) &= -\frac{\eta_1(\vartheta,\varphi)}{r'(1)}\,,
\end{aligned}$$

and

$$\begin{aligned}
\boldsymbol{\nu}_{1,0}(\vartheta,\varphi) &= \frac{\eta_0(\vartheta,\varphi)}{\psi\left(0,\frac{\pi}{2}-\varphi\right)}\Big(\Big(1+\frac{r(0)\,\boldsymbol{z}''(0)\cdot\boldsymbol{\zeta}(0,\varphi)}{|\boldsymbol{z}'(0)|^2}\Big)\boldsymbol{t}(0)+\frac{r(0)\,\boldsymbol{z}''(0)\cdot\boldsymbol{t}(0)}{|\boldsymbol{z}'(0)|^2}\,\boldsymbol{\zeta}(0,\varphi)\Big),\\
\boldsymbol{\nu}_{1,1}(\vartheta,\varphi) &= \frac{\eta_1(\vartheta,\varphi)}{\psi\left(1,\varphi\right)}\Big(\Big(1+\frac{r(1)\,\boldsymbol{z}''(1)\cdot\boldsymbol{\zeta}(1,\varphi)}{|\boldsymbol{z}'(1)|^2}\Big)\boldsymbol{t}(1)+\frac{r(1)\,\boldsymbol{z}''(1)\cdot\boldsymbol{t}(1)}{|\boldsymbol{z}'(1)|^2}\,\boldsymbol{\zeta}(1,\varphi)\Big),\\
\boldsymbol{\nu}_{2,0}(\vartheta,\varphi) &= -\frac{r(0)\,\eta_0(\vartheta,\varphi)}{\psi\left(0,\frac{\pi}{2}-\varphi\right)\,|\boldsymbol{z}'(0)|}\,\boldsymbol{\zeta}(0,\varphi)\,,\\
\boldsymbol{\nu}_{2,1}(\vartheta,\varphi) &= -\frac{r(1)\,\eta_1(\vartheta,\varphi)}{\psi\left(1,\varphi\right)\,|\boldsymbol{z}'(1)|}\,\boldsymbol{\zeta}(1,\varphi)\,.
\end{aligned}$$

Finally, the perturbation of the parametrization of the caps from (12b) *and* (12c) *is given by*

$$\begin{aligned}
\boldsymbol{\xi}_{\mathrm{start},\boldsymbol{\delta}}(\vartheta,\varphi) &= \boldsymbol{\xi}_{\mathrm{start}}(\vartheta,\varphi) + \alpha_0(\vartheta)\,\boldsymbol{\delta}'(0) + \boldsymbol{\beta}_0(\vartheta,\varphi)\cdot\boldsymbol{\delta}'(0)\,\boldsymbol{t}(0) + \mathrm{o}\left(\|\boldsymbol{\delta}\|_{1,\infty}\right),\\
\boldsymbol{\xi}_{\mathrm{end},\boldsymbol{\delta}}(\vartheta,\varphi) &= \boldsymbol{\xi}_{\mathrm{end}}(\vartheta,\varphi) + \alpha_1(\vartheta)\,\boldsymbol{\delta}'(1) + \boldsymbol{\beta}_1(\vartheta,\varphi)\cdot\boldsymbol{\delta}'(1)\,\boldsymbol{t}(1) + \mathrm{o}\left(\|\boldsymbol{\delta}\|_{1,\infty}\right)
\end{aligned}$$

as $\|\boldsymbol{\delta}\|_{1,\infty} \to 0$, *where*

$$\begin{aligned}
\alpha_0(\vartheta) &= -\frac{\cos(\vartheta)}{|\boldsymbol{z}'(0)|}\,, \quad \boldsymbol{\beta}_0(\vartheta,\varphi) = -\frac{\boldsymbol{\xi}_{\mathrm{start}}(\vartheta,\varphi)}{|\boldsymbol{z}'(0)|}\,,\\
\alpha_1(\vartheta) &= \frac{\cos(\vartheta)}{|\boldsymbol{z}'(1)|}\,, \quad \boldsymbol{\beta}_1(\vartheta,\varphi) = -\frac{\boldsymbol{\xi}_{\mathrm{end}}(\vartheta,\varphi)}{|\boldsymbol{z}'(1)|}\,.
\end{aligned}$$

From Lemma 3.6, we can immediately obtain an explicit formula for $\boldsymbol{h}$.

Corollary 3.7 *The function* $\boldsymbol{h}$ *from Theorem 3.5 is given by* $\boldsymbol{h}(x) = \boldsymbol{h}_{\mathrm{body}}(\boldsymbol{x})$ *for* $\boldsymbol{x} = \boldsymbol{x}_{\mathrm{body}}(\tau,\varphi)$ *and by* $\boldsymbol{h}(\boldsymbol{x}) = \boldsymbol{h}_\ell(\boldsymbol{x})$ *for* $\boldsymbol{x} = \boldsymbol{x}_\ell(\vartheta,\varphi)$, $\ell \in \{\mathrm{start},\mathrm{end}\}$, *where*

$$\begin{aligned}
\boldsymbol{h}_{\mathrm{body}}(\boldsymbol{x}) &= \boldsymbol{\delta}(\tau) - \frac{r(\tau)\,\boldsymbol{\delta}'(\tau)\cdot\boldsymbol{\zeta}(\tau,\varphi)}{|\boldsymbol{z}'(\tau)|}\,\boldsymbol{t}(\tau) + \varepsilon(\tau)\,\boldsymbol{\zeta}(\tau,\varphi)\,,\\
\boldsymbol{h}_{\mathrm{start}}(\boldsymbol{x}) &= \boldsymbol{\delta}(0) + \rho_0(\vartheta,\varphi)\,\alpha_0(\vartheta)\,\boldsymbol{\delta}'(0) + \rho_0(\vartheta,\varphi)\,\boldsymbol{\beta}_0(\vartheta,\varphi)\cdot\boldsymbol{\delta}'(0)\,\boldsymbol{t}(0)\\
&\quad + \Big(\sum_{j=0}^{1}\mu_{j,0}(\vartheta,\varphi)\,\varepsilon^{(j)}(0) + \sum_{j=1}^{2}\boldsymbol{\nu}_{j,0}(\vartheta,\varphi)\cdot\boldsymbol{\delta}^{(j)}(0)\Big)\boldsymbol{\xi}_{\mathrm{start}}(\vartheta,\varphi)\,,\\
\boldsymbol{h}_{\mathrm{end}}(\boldsymbol{x}) &= \boldsymbol{\delta}(1) + \rho_1(\vartheta,\varphi)\,\alpha_1(\vartheta)\,\boldsymbol{\delta}'(1) + \rho_1(\vartheta,\varphi)\,\boldsymbol{\beta}_1(\vartheta,\varphi)\cdot\boldsymbol{\delta}'(1)\,\boldsymbol{t}(1)\\
&\quad + \Big(\sum_{j=0}^{1}\mu_{j,1}(\vartheta,\varphi)\,\varepsilon^{(j)}(1) + \sum_{j=1}^{2}\boldsymbol{\nu}_{j,1}(\vartheta,\varphi)\cdot\boldsymbol{\delta}^{(j)}(1)\Big)\boldsymbol{\xi}_{\mathrm{end}}(\vartheta,\varphi)\,,
\end{aligned}$$

with the coefficient functions defined in Lemma 3.6.

Proof: By definition,

$$\boldsymbol{x}_{\ell,(\boldsymbol{\delta},\varepsilon)} = \boldsymbol{x}_\ell + \boldsymbol{h}\circ\boldsymbol{x}_\ell + \mathrm{o}\left(\|\boldsymbol{\delta}\|_{2,\infty} + \|\varepsilon\|_{1,\infty}\right), \qquad \ell \in \{\mathrm{body},\mathrm{start},\mathrm{end}\}\,.$$

for $\|\boldsymbol{\delta}\|_{2,\infty}$, $\|\varepsilon\|_{1,\infty} \to 0$. We have

$$\begin{aligned}\boldsymbol{x}_{\mathrm{body},(\boldsymbol{\delta},\varepsilon)}(\tau,\varphi) \;=\; & \boldsymbol{z}(\tau) + \boldsymbol{\delta}(\tau) + \varepsilon(\tau)\boldsymbol{\zeta}(\tau,\varphi) \\ & + r(\tau)\,\left(\cos(\varphi)\,\boldsymbol{n}_{\boldsymbol{\delta}}(\tau) + \sin(\varphi)\,\boldsymbol{b}_{\boldsymbol{\delta}}(\tau)\right) + \mathrm{o}\left(\|\boldsymbol{\delta}\|_{1,\infty} + \|\varepsilon\|_{\infty}\right),\end{aligned}$$

where $\tau \in [0,1]$ and $\varphi \in (-\pi,\pi]$. Inserting the asymptotic expansions from (11) then gives the result of the corollary for $\boldsymbol{x} = \boldsymbol{x}_{\mathrm{body}}(\tau,\varphi)$. Likewise,

$$\begin{aligned}\boldsymbol{x}_{\ell,(\boldsymbol{\delta},\varepsilon)}(\vartheta,\varphi) \;=\; & \boldsymbol{x}_{\ell}(\vartheta,\varphi) + \rho_{\tau}(\vartheta,\varphi)\,\left(\boldsymbol{\xi}_{\ell,\boldsymbol{\delta}}(\vartheta,\varphi) - \boldsymbol{\xi}_{\ell}(\vartheta,\varphi)\right) \\ & + \boldsymbol{\xi}_{\ell}(\vartheta,\varphi)\,\left(\rho_{\tau,(\boldsymbol{\delta},\varepsilon)}(\vartheta,\varphi) - \rho_{\tau}(\vartheta,\varphi)\right) + \mathrm{o}\left(\|\boldsymbol{\delta}\|_{2,\infty} + \|\varepsilon\|_{1,\infty}\right),\end{aligned}$$

where $(\ell,\tau) \in \{(\mathrm{start},0),(\mathrm{end},1)\}$, $\vartheta \in [0,\pi/2]$ and $\varphi \in (-\pi,\pi]$. The remaining assertion follows from Lemma 3.6. ∎

Proof:[Proof of Theorem 3.5] In order for $F'[\partial D]\boldsymbol{h}_{(\boldsymbol{\delta},\varepsilon)}$ to exist and to satisfy the formula $F'[\partial D]\boldsymbol{h}_{(\boldsymbol{\delta},\varepsilon)} = \boldsymbol{E}'^{\infty}_{(\boldsymbol{\delta},\varepsilon)}$, the vector field $\boldsymbol{h}_{(\boldsymbol{\delta},\varepsilon)}$ from (17) needs to be extended to a compact neighborhood of ∂D. Here, we first extend it constantly to a tubular neighborhood of ∂D and multiply with a smooth cut-off function afterwards so that the extension has compact support. For this purpose, let $I \subset \mathbb{R}$ be a small neighborhood of 0 and denote by $\mathcal{S}_{\sigma}$ the C^1-smooth surface generated by $(\boldsymbol{z}, r+\sigma)$, for $\sigma \in I$. Then, $\mathcal{U} = \bigcup_{\sigma\in I}\mathcal{S}_{\sigma}$ is an open neighborhood of ∂D. Let

$$\Psi(\boldsymbol{x},\sigma) \;=\; \boldsymbol{x} + \boldsymbol{h}_{(\boldsymbol{0},\sigma)}(\boldsymbol{x})\,, \qquad (\boldsymbol{x},\sigma) \in \partial D \times I\,.$$

For any $(\boldsymbol{x},\sigma) \in \partial D \times I$, it holds that $\Psi(\boldsymbol{x},\sigma) \in S_{\sigma}$. Moreover, Ψ is continuous. Now, let $\boldsymbol{x}^* \in \partial D$ and let $U \subset \partial D$ be a relative open and sufficiently small neighborhood of $\boldsymbol{x}^*$ in ∂D. By the definition of a regular C^1-smooth domain, there exists an open $V \subset \mathbb{R}^2$ and a regular C^1 parametrization $\alpha : V \to U$. Let $\boldsymbol{y}^* \in V$ be such that $\alpha(\boldsymbol{y}^*) = \boldsymbol{x}^*$. With $\widetilde{\Psi}(\boldsymbol{y},\sigma) = \Psi(\alpha(\boldsymbol{y}),\sigma)$ for $(\boldsymbol{y},\sigma) \in V \times I$, we obtain for $\ell \in \{\mathrm{body},\mathrm{start},\mathrm{end}\}$

$$\widetilde{\Psi}(\boldsymbol{y},\sigma) = \alpha(\boldsymbol{y}) + \boldsymbol{h}_{(\boldsymbol{0},\sigma)}(\alpha(\boldsymbol{y})) = \boldsymbol{x}_{\ell,(\boldsymbol{0},\sigma)}(\boldsymbol{x}_{\ell}^{-1}(\alpha(\boldsymbol{y})))\,, \quad \alpha(\boldsymbol{y}) \in \mathcal{S}_{\ell} \cap U\,.$$

Then, since $\boldsymbol{h}(\boldsymbol{0},0)$ vanishes, it holds that

$$\begin{aligned}\frac{\partial\widetilde{\Psi}(\boldsymbol{y}^*,0)}{\partial y_j} \;&=\; \frac{\partial\alpha(\boldsymbol{y}^*)}{\partial y_j}\,, \\ \frac{\partial\widetilde{\Psi}(\boldsymbol{y}^*,0)}{\partial\sigma} \;&=\; \lim_{\sigma\to 0}\frac{\Psi(\boldsymbol{x}^*,\sigma)-\Psi(\boldsymbol{x}^*,0)}{\sigma} \;=\; \lim_{\sigma\to 0}\frac{\boldsymbol{h}_{(\boldsymbol{0},\sigma)}(\boldsymbol{x}^*)}{\sigma} \;=\; \lim_{\sigma\to 0}\frac{\widetilde{\boldsymbol{h}}(\boldsymbol{x}^*)}{\sigma}\,,\end{aligned}$$

where $\widetilde{\boldsymbol{h}}$ denotes the linearization of $\boldsymbol{h}_{(0,\sigma)}$ with respect to σ. The regularity of α implies that $\partial_{y_1}\widetilde{\Psi}(\boldsymbol{y}^*,0)\times\partial_{y_2}\widetilde{\Psi}(\boldsymbol{y}^*,0) = c\boldsymbol{\nu}$ for some function $c \neq 0$. An inspection of $\widetilde{\boldsymbol{h}}$ in Corollary 3.7, together with the fact that the Jacobian $J_{\widetilde{\Psi}}$ of $\widetilde{\Psi}$ satisfies $\det(J_{\widetilde{\Psi}}) = (\partial_{y_1}\widetilde{\Psi}(\boldsymbol{y}^*,0)\times\partial_{y_2}\widetilde{\Psi}(\boldsymbol{y}^*,0))\cdot\widetilde{\boldsymbol{h}} \neq 0$ yields that $J_{\widetilde{\Psi}}$ is invertible. By the inverse function theorem Ψ defines a local diffeomorphism around $(\boldsymbol{x}^*,0)$. Due to the compactness of ∂D, it follows that there exists a sufficiently small I such that $\Psi : \partial D \times I \to \mathcal{U}$ is bijective. The constant extension of $\boldsymbol{h}_{(\boldsymbol{\delta},\varepsilon)}$ to $\mathcal{U}$ is now given by

$$\boldsymbol{h}_{(\boldsymbol{\delta},\varepsilon)}(\boldsymbol{u}) \;=\; \boldsymbol{h}_{(\boldsymbol{\delta},\varepsilon)}(\boldsymbol{x})\,, \qquad \boldsymbol{u} = \Psi(\boldsymbol{x},\sigma) \in \mathcal{U}\,.$$

Multiplication of $\boldsymbol{h}_{(\boldsymbol{\delta},\varepsilon)}$ with a smooth cut-off function provides a compact support in $\mathcal{U}$. For the extended and truncated $\boldsymbol{h}_{(\boldsymbol{\delta},\varepsilon)}$ we can now apply (6), what yields that

$$\lim_{\|\boldsymbol{h}_{(\boldsymbol{\delta},\varepsilon)}\|_{1,\infty}\to 0}\frac{\left\|F(\boldsymbol{z}+\boldsymbol{\delta},r+\varepsilon)-F(\boldsymbol{z},r)-\boldsymbol{E}'^{\infty}_{(\boldsymbol{\delta},\varepsilon)}\right\|_{L^2_t(\mathbb{S}^2)}}{\|\boldsymbol{h}_{(\boldsymbol{\delta},\varepsilon)}\|_{1,\infty}} \;=\; 0\,,$$

where $\boldsymbol{E}'_{(\boldsymbol{\delta},\varepsilon)}$ denotes the solution of (3a) together with (7) in the case of a perfect conducting obstacle and of (4a) together with (8) in the case of a penetrable obstacle, with $\boldsymbol{\eta}$ replaced by $\boldsymbol{h}_{(\boldsymbol{\delta},\varepsilon)}$. From the well-posedness of these exterior boundary value problems, we furthermore conclude

$$\left\|\boldsymbol{E}'^{\infty}_{(\boldsymbol{\delta},\varepsilon)} - \boldsymbol{E}'^{\infty}\right\|_{L^2_t(\mathbb{S}^2)} \leq C \left\|\boldsymbol{h}_{(\boldsymbol{\delta},\varepsilon)} - \boldsymbol{h}\right\|_{1,\infty}.$$

Thus,

$$\begin{aligned}
&\|F(\boldsymbol{z}+\boldsymbol{\delta}, r+\varepsilon) - F(\boldsymbol{z}, r) - \boldsymbol{E}'^{\infty}\|_{L^2_t(\mathbb{S}^2)} \\
&\quad\leq \left\|F(\boldsymbol{z}+\boldsymbol{\delta}, r+\varepsilon) - F(\boldsymbol{z}, r) - \boldsymbol{E}'^{\infty}_{(\boldsymbol{\delta},\varepsilon)}\right\|_{L^2_t(\mathbb{S}^2)} + \left\|\boldsymbol{E}'^{\infty}_{(\boldsymbol{\delta},\varepsilon)} - \boldsymbol{E}'^{\infty}\right\|_{L^2_t(\mathbb{S}^2)} \\
&\quad\leq \mathrm{o}\left(\|\boldsymbol{h}_{(\boldsymbol{\delta},\varepsilon)}\|_{1,\infty}\right) + C\,\|\boldsymbol{h}_{(\boldsymbol{\delta},\varepsilon)} - \boldsymbol{h}\|_{1,\infty}
\end{aligned}$$

as $\|\boldsymbol{h}_{(\boldsymbol{\delta},\varepsilon)}\|_{1,\infty} \to 0$. By the definition of $\boldsymbol{h}_{(\boldsymbol{\delta},\varepsilon)}$ and by (18), we see that both terms are of order $\mathrm{o}(\|\boldsymbol{\delta}\|_{2,\infty} + \|\varepsilon\|_{1,\infty})$ as these norms tend to 0, which finishes the proof. ∎

4 Numerical implementation and examples

The challenge in reconstructing a tubular scatterer from its far field data consists in solving the nonlinear ill-posed operator equation (9). For this purpose, we study the discrepancy between the given far field data $\boldsymbol{E}^{\infty}$ and the far field $F(\boldsymbol{z}, r)$ generated by a tubular scatterer parametrized by $(\boldsymbol{z}, r) \in \mathcal{M}$ with $\mathcal{M}$ as in (16). Our approach in solving (9) is to minimize this discrepancy in the set $\mathcal{M}$. Due to the ill-posed nature of the problem we add suitable regularization terms to the discrepancy and then minimize this regularized functional using the Gauss–Newton method.

Inspired by previous work using asymptotic scattering models for thin tubular objects [1,5,16], we solve the minimization problem

$$J(\boldsymbol{z}, r) = \|F(\boldsymbol{z}, r) - \boldsymbol{E}^{\infty}\|^2_{L^2_t(\mathbb{S}^2)} + \alpha_1\,\Psi_1(\boldsymbol{z}) + \alpha_2\,\Psi_2(\boldsymbol{z}) + \alpha_3\,\Psi_3(r) \to \min, \tag{19}$$

for $(\boldsymbol{z}, r) \in \mathcal{M}$ with regularization parameters $\alpha_j > 0$, $j = 1, 2, 3$. The regularization terms, which we discuss in more detail below, penalize unfavorable characteristics of the spine curve $\boldsymbol{z}$ and the radius function r during the optimization.

The first regularization term is the total curvature of the spine curve $\boldsymbol{z}$, which is given by

$$\Psi_1(\boldsymbol{z}) = \int_0^1 \kappa^2(\tau)|\boldsymbol{z}'(\tau)|\mathrm{d}\tau, \quad \text{with curvature } \kappa(\tau) = \frac{|\boldsymbol{z}'(\tau)\times\boldsymbol{z}''(\tau)|}{|\boldsymbol{z}'(\tau)|^3}.$$

To define the second penalty term, aimed at ensuring a close to uniform segmentation of the parameter interval, we choose $n \in \mathbb{N}$ knots t_j, $j = 1, \ldots, n$, on the parameter interval $[0, 1]$. The regularization term is then defined by

$$\Psi_2(\boldsymbol{z}) = \sum_{j=1}^{n-1} \left| \frac{1}{n-1} \int_0^1 |\boldsymbol{z}'(\tau)|\,\mathrm{d}\tau - \int_{t_j}^{t_{j+1}} |\boldsymbol{z}'(\tau)|\,\mathrm{d}\tau \right|^2.$$

Finally, the third term, penalizing large variations of the radius function r, is defined as

$$\Psi_3(r) = \int_0^1 |r'(\tau)|^2\,\mathrm{d}\tau.$$

In each step of the Gauss–Newton scheme, an update to the current iterate is computed. In this update step we impose two additional constraints. On the one hand, we require r to remain positive and on the other hand, we require the condition

$$r(t)\|\kappa\|_{C[0,1]} < 1, \quad t \in [0, 1],$$

to hold. As described in [17, Thm. 1], this condition on the curvature κ and radius r guarantees the tube to have no local self-intersections.

In the implementation, we represent $\boldsymbol{z}$ by a 3rd-order B-spline curve defined by $n+2$ control points and the radius function by a cubic spline using the knots t_j as interpolation points. Applying the Gauss–Newton method to solve (19) involves the computation of the Fréchet derivative of J. Formulas for the derivative of Ψ_1 and Ψ_2 in the context of the Gauss–Newton scheme are given in [16, Lem. 4.5]. The derivative of Ψ_3 is easy to compute. To obtain the Fréchet derivative of the far field map, the problems (3) and (3a) together with the boundary condition (7) need to be solved in the case of a perfectly conducting scatterer. For a penetrable scatterer, the problems (4) as well as (4a) together with the boundary condition (8) need to be solved.

We translate these exterior boundary value problems into equivalent integral equations which we solve by using the boundary element method. Let

$$\Phi_k(\boldsymbol{x},\boldsymbol{y}) = \frac{\mathrm{e}^{\mathrm{i}k|\boldsymbol{x}-\boldsymbol{y}|}}{4\pi|\boldsymbol{x}-\boldsymbol{y}|}\,, \qquad \boldsymbol{x}\neq\boldsymbol{y}\,,$$

denote the fundamental solution of the Helmholtz equation $\Delta u + k^2 u = 0$ in $\mathbb{R}^3\setminus\{\boldsymbol{y}\}$ for the wave number k. For a smooth scalar- and vector-valued density φ and $\boldsymbol{\varphi}$, the scalar- and vector-valued single layer potentials SL_k and $\mathbf{SL}_k$ are given by

$$\mathrm{SL}_k\,\varphi(\boldsymbol{x}) \;=\; \int_{\partial D} \Phi_k(\boldsymbol{x},\boldsymbol{y})\varphi(\boldsymbol{y})\,\mathrm{d}s(\boldsymbol{y}) \quad\text{and}\quad \mathbf{SL}_k\,\boldsymbol{\varphi}(\boldsymbol{x}) \;=\; \int_{\partial D} \Phi_k(\boldsymbol{x},\boldsymbol{y})\boldsymbol{\varphi}(\boldsymbol{y})\,\mathrm{d}s(\boldsymbol{y})\,,$$

where $\boldsymbol{x}\in\mathbb{R}^3\setminus\partial D$. The potentials SL_k and $\mathbf{SL}_k$ extend to continuous operators from $H^{-1/2}(\partial D,\mathbb{C}^m)$ to $H^1_{\mathrm{loc}}(\mathbb{R}^3,\mathbb{C}^m)$ for $m=1$ and $m=3$, respectively. The electric and magnetic potentials

$$\boldsymbol{\mathcal{E}}_k\,\boldsymbol{\varphi} = \mathrm{i}k\;\mathbf{SL}_k\,\boldsymbol{\varphi} - \frac{1}{\mathrm{i}k}\;\mathbf{grad}\,\mathrm{SL}_k(\mathrm{Div}\,\boldsymbol{\varphi}) \quad\text{and}\quad \boldsymbol{\mathcal{H}}_k = \mathbf{curl}\,\mathbf{SL}_k\,\boldsymbol{\varphi}$$

are both well-defined continuous linear operators mapping from $H^{-1/2}(\mathrm{Div},\partial D)$ to $H(\mathbf{curl}^2,D)$ and to $H_{\mathrm{loc}}(\mathbf{curl}^2,\mathbb{R}^3\setminus\overline{D})$, respectively (see [3, Sec. 4]). The electromagnetic boundary operators $\mathbf{S}_k$, $\mathbf{C}_k$: $H^{-1/2}(\mathrm{Div},\partial D)\to H^{-1/2}(\mathrm{Div},\partial D)$ are obtained by averaging tangential traces of the potentials,

$$\mathbf{S}_k = \frac{1}{2}\left(\gamma_t^+\,\boldsymbol{\mathcal{E}}_k + \gamma_t^-\,\boldsymbol{\mathcal{E}}_k\right), \quad \mathbf{C}_k = \frac{1}{2}\left(\gamma_t^+\,\boldsymbol{\mathcal{H}}_k + \gamma_t^-\,\boldsymbol{\mathcal{H}}_k\right).$$

Here, the superscript "+" indicates a trace taken from $\mathbb{R}^3\setminus\overline{D}$, while the superscript "−" indicates a trace taken from inside D. The boundary operators satisfy the jump relations (see [3, Thm. 7])

$$\gamma_t^\pm\,\boldsymbol{\mathcal{E}}_k = \mathbf{S}_k\,, \quad \gamma_N^\pm\,\boldsymbol{\mathcal{E}}_k = \mp\frac{1}{2}I + \mathbf{C}_k\,, \quad \gamma_t^\pm\,\boldsymbol{\mathcal{H}}_k = \mp\frac{1}{2}I + \mathbf{C}_k\,, \quad \gamma_N^\pm\,\boldsymbol{\mathcal{H}}_k = \mathbf{S}_k\,.$$

We also introduce the multitrace operator

$$\mathbf{A}_k : (H^{-1/2}(\mathrm{Div},\partial D))^2 \to (H^{-1/2}(\mathrm{Div},\partial D))^2\,, \quad \mathbf{A}_k \;=\; \begin{bmatrix} \mathbf{C}_k & \mathbf{S}_k \\ -\,\mathbf{S}_k & \mathbf{C}_k \end{bmatrix}.$$

To compute the scattered field or its domain derivative for the perfect conductor problem, we use the regularized combined field integral equation (CFIE). Defining the regularization operator $\mathbf{R}=\mathbf{S}_{ik}$, the equation is

$$\left(\frac{1}{2}I + \mathbf{C}_k - \mathbf{R}\,\mathbf{S}_k\right)\boldsymbol{\Lambda} \;=\; \left(\mathbf{S}_k + \mathbf{R}\left(\frac{1}{2}I + \mathbf{C}_k\right)\right)\boldsymbol{f}\,, \tag{20}$$

where $\boldsymbol{f}$ is given by the right-hand side of (3b) or (7). The solution of (20) is equal to the magnetic tangential trace on ∂D of the corresponding radiating field in $\mathbb{R}^3 \setminus \overline{D}$, i.e., it holds

$$\boldsymbol{\Lambda} = \gamma_N^+ \boldsymbol{E}^s \text{ for } \boldsymbol{f} \text{ as in (3b)} \quad \text{and} \quad \boldsymbol{\Lambda} = \gamma_N^+ \boldsymbol{E}' \text{ for } \boldsymbol{f} \text{ as in (7)}.$$

The corresponding radiating electric field is $\boldsymbol{\mathcal{E}}_k \boldsymbol{\Lambda}$. This version of the CFIE has the advantage of being well-conditioned as well as neither suffering from spurious frequencies nor having the "low-frequency problem" [6].

For the penetrable scatterer, we instead use a variant of the well-known PMCHWT integral equation which uses the exterior traces of the scattered electric and magnetic fields as the unknowns [3,4]. For abbreviation, we denote by $k_1 = \omega\sqrt{\varepsilon_1 \mu_1}$ the wave number in the interior and by $\varepsilon_r = \varepsilon_1/\varepsilon_0$ and $\mu_r = \mu_1/\mu_0$ the relative electric permittivity and relative magnetic permeability, respectively. The integral equation now reads

$$\left(S^{-1}\,\mathbf{A}_{k_1}\,S + \mathbf{A}_k\right)\begin{bmatrix}\boldsymbol{\Lambda}\\ \boldsymbol{\Upsilon}\end{bmatrix} = \left(S^{-1}\,\mathbf{A}_{k_1}\,S - \frac{1}{2}I\right)\begin{bmatrix}\boldsymbol{f}\\ \boldsymbol{g}\end{bmatrix}, \quad \text{with} \quad S = \begin{bmatrix}1 & 0\\ 0 & \sqrt{\frac{\mu_r}{\varepsilon_r}}\end{bmatrix} \tag{21}$$

and the functions $\boldsymbol{f}$, $\boldsymbol{g}$ given by the right hand sides of (4b) and (8), respectively. The integral equation is uniquely solvable (see [4, Cor. 6.4]) with the unknown functions given by

$$\begin{bmatrix}\boldsymbol{\Lambda}\\ \boldsymbol{\Upsilon}\end{bmatrix} = \begin{bmatrix}\gamma_t^+ \boldsymbol{E}^s\\ \gamma_t^+ \boldsymbol{H}^s\end{bmatrix} \text{ for } \begin{bmatrix}\boldsymbol{f}\\ \boldsymbol{g}\end{bmatrix} \text{ as in (4b)} \quad \text{and} \quad \begin{bmatrix}\boldsymbol{\Lambda}\\ \boldsymbol{\Upsilon}\end{bmatrix} = \begin{bmatrix}\gamma_t^+ \boldsymbol{E}'\\ \gamma_t^+ \boldsymbol{H}'\end{bmatrix} \text{ for } \begin{bmatrix}\boldsymbol{f}\\ \boldsymbol{g}\end{bmatrix} \text{ as in (8)}.$$

The radiating fields and their far field patterns may be obtained from the Stratton–Chu representation formula.

The discretization of these boundary integral equations is carried out using the `bempp-cl` boundary element method library (see https://bempp.com). In this library, the function spaces are discretized using the Rao–Wilton–Glisson (RWG) and Buffa–Christiansen (BC) finite element families as detailed in [20]. Implementations of all integral operators introduced above are available, and data sparse representations can be assembled by employing the fast multipole method.

The operations and surface differential operators occurring in (7) and (8) are not all readily available in the library and hence require additional implementation. Using the formulas

$$\boldsymbol{E}_{\boldsymbol{\nu}} = \boldsymbol{\nu} \cdot \boldsymbol{E} = -\frac{1}{\mathrm{i}k}\operatorname{Div}(\gamma_t \boldsymbol{H}) \qquad \text{and} \qquad \mathbf{Curl}\,(\boldsymbol{h}_{\boldsymbol{\nu}} \boldsymbol{E}_{\boldsymbol{\nu}}) = \mathbf{Grad}(\boldsymbol{h}_{\boldsymbol{\nu}} \boldsymbol{E}_{\boldsymbol{\nu}}) \times \boldsymbol{\nu}\,,$$

we may compute all quantities occurring in the boundary and transmission conditions (7), (8) from the total fields of the corresponding direct scattering problem. The surface gradient **Grad** is available as an implemented operator in `bempp-cl` while the surface divergence can be represented in weak form via the partial integration formula

$$\int_{\partial D} v \operatorname{Div} \boldsymbol{U}\, \mathrm{d}s = -\int_{\partial D} \boldsymbol{U} \cdot \mathbf{Grad}\, v\, \mathrm{d}s\,.$$

Further operations such as the rotation operator $\cdot \times \boldsymbol{\nu}$ and the product of two boundary functions are implemented using suitable projections on the relevant boundary element spaces.

For our numerical experiments, we consider the scattering of a plane wave

$$(\boldsymbol{E}^i, \boldsymbol{H}^i) = \left(\boldsymbol{p}, \sqrt{\frac{\varepsilon_0}{\mu_0}}\,\boldsymbol{d} \times \boldsymbol{p}\right) \mathrm{e}^{\mathrm{i}k\boldsymbol{x}\cdot\boldsymbol{d}}, \qquad \boldsymbol{d} = \frac{1}{\sqrt{3}}\begin{bmatrix}1\\1\\1\end{bmatrix}, \quad \boldsymbol{p} = \begin{bmatrix}1\\0\\-1\end{bmatrix},$$

from a tubular obstacle D. The vector $\boldsymbol{d} \in S^2$ is the direction of propagation and the vector $\boldsymbol{p} \in \mathbb{C}^3 \setminus \{0\}$ denotes the polarization of the plane wave. The electric far field pattern corresponding

to this pair of incident plane waves is denoted by $\boldsymbol{E}^\infty$. We further perturb the electric far field pattern $\boldsymbol{E}^\infty$ by some additive complex-valued random noise with noise level $\delta > 0$. The given data for the reconstruction is thus $\boldsymbol{E}^{\infty,\delta}$ satisfying

$$\frac{\left\|\boldsymbol{E}^\infty - \boldsymbol{E}^{\infty,\delta}\right\|_{L_t^2(\mathbb{S}^2)}}{\left\|\boldsymbol{E}^\infty\right\|_{L_t^2(\mathbb{S}^2)}} = \delta\,.$$

The obstacle D is represented by functions $(\boldsymbol{z}, r) \in \mathcal{M}$ as detailed in the examples below. For representing the iterates during the reconstruction we use a different discretization than in the simulation for the true scattering object D. This is supposed to reduce the risk of inverse crime. We use the generalized minimal residual (GMRES) method to approximate the solution to the system of linear equations resulting from the discretization of the CFIE in (20) and the PMCHWT integral equation in (21). For the GMRES method we pick the tolerance 1e–5 and do not use any restarts. The Gauss–Newton iteration terminates when either the relative residual becomes smaller than the applied noise level or when the relative movement of the spine curve and the relative change of the radius function, which are computed by the norm of the respective update divided by the norm of the corresponding previous data, fall below a given tolerance. In all subsequent examples, a tolerance of 1% for both the relative movement and the relative radius change is selected. For each example we provide a convergence history together with a graph of the relative residual plotted against the iteration number. Each plot of the convergence history features the true scatterer in faded blue together with projections onto two surrounding planes in faded gray. The current iterate is found in solid blue with its projections in solid gray. The chosen iterates are indicated in the graph by dashed lines that highlight the iteration number and the associated relative residual.

Example 4.1 *We consider a perfectly conducting obstacle D defined by a 3rd-degree B-spline curve with control points $\boldsymbol{c}_j = (\cos(j\pi/5), \sin(j\pi/5), j/5)^\top$, $j = 0, \dots, 4$. The radius function $r = 3/20 \exp(\sin(\cdot))$ is represented by a cubic spline with the distinct knots of the B-spline as the interpolation points. We choose the material parameters $\varepsilon_0 = \mu_0 = 1$ and the angular frequency $\omega = 2$. Discretizing the surface leads to a mesh and a corresponding RWG finite element family with 9882 degrees of freedom (DOFs).*

For the reconstruction, we choose a B-spline spine curve of degree 3 defined by 7 control points and knots $t_j = j/6$, $j = 0, \dots, 6$. The radial function is represented by a cubic spline with these points t_j as the interpolation points. For the initial guess, the spine curve is chosen straight and the radius function constant. In each iteration, the RWG space discretization of the corresponding mesh has 6426 DOFs. The regularization parameters are chosen as $\alpha_1 = 25/4$, $\alpha_2 = 64$, $\alpha_3 = 36$. For solving the boundary integral equations from (20), the GMRES method requires between 22 and 35 iterations. Starting with a relative residual of approximately 82.4% the Gauss–Newton iteration terminates after 9 iterations with a relative residual of around 1.5%. The results for the reconstruction are shown in Figure 4.

Example 4.2 *We consider a penetrable obstacle, where the material parameters are chosen as $\varepsilon_1 = 2$, $\mu_1 = 1$, i.e., $\varepsilon_r = 2$, $\mu_r = 1$, and the angular frequency as $\omega = 2\sqrt{2}$. In this example, the spine curve of the true scatterer $\boldsymbol{z}$ is the 3rd-degree B-spline curve with control points $\boldsymbol{c}_j = (\cos(2j\pi/5), \sin(2j\pi/5), 3j/5)^\top$, $j = 0, \dots, 4$. This results in a helical object with one complete turn. As before, we consider the radius function $r = 3/20 \exp(\sin(\cdot))$, which is represented by a cubic spline with the distinct knots of the B-spline as the interpolation points. The finite element space of RWG and BC functions, which is used for computing the exact far field data, has 19764 DOFs in total.*

To represent the domains in the reconstruction, we use 8 control points and the knots $t_j = j/7$, $j = 0, \dots, 7$. Here, throughout the whole reconstruction we pick finite element spaces of RWG and BC

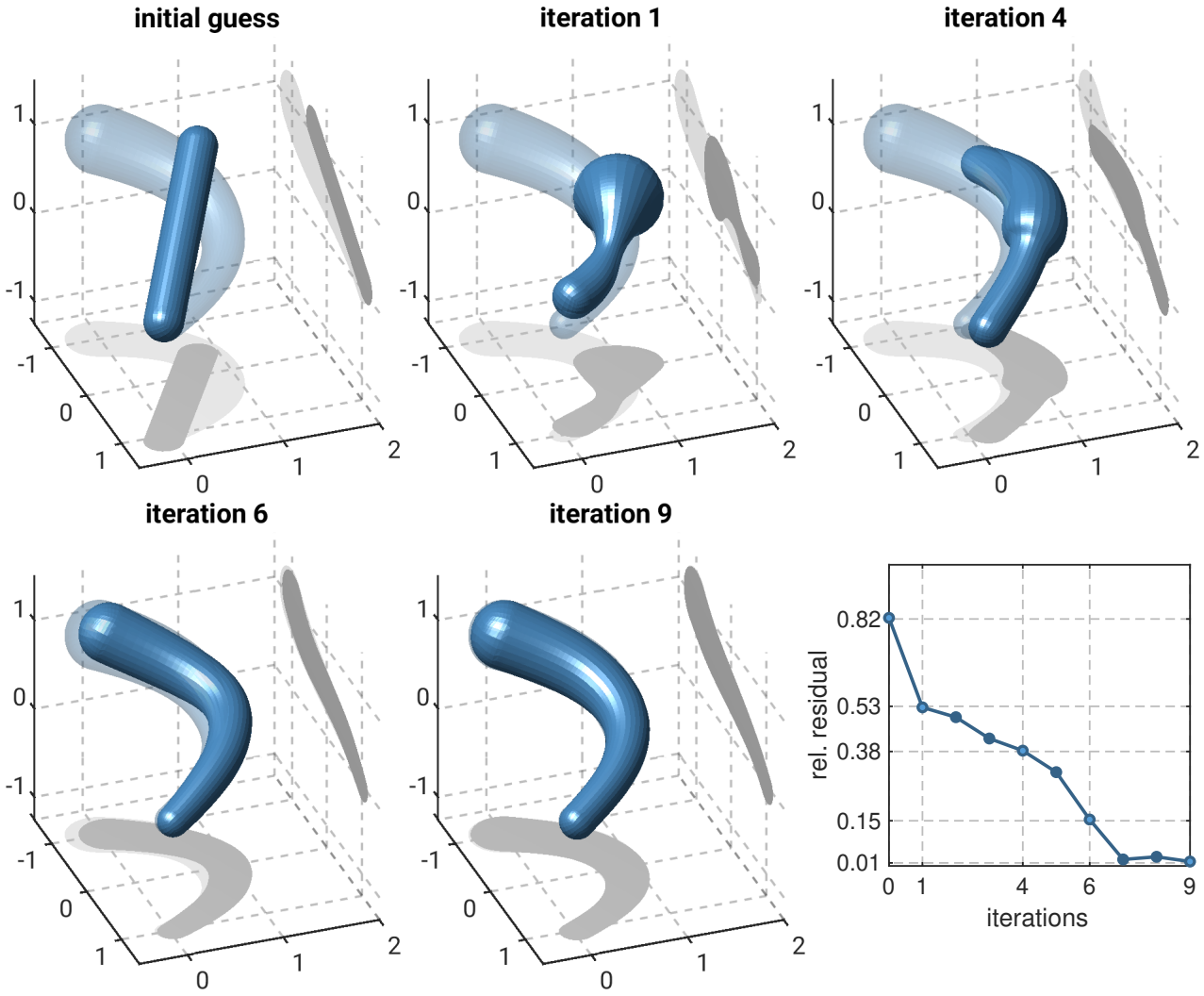

Figure 2: Top-left to bottom-center: The initial guess, samples of the reconstruction and the final reconstruction for Example 4.1 are depicted. The exact obstacle is displayed slightly transparent as a comparison for each iteration. Bottom-right: The relative residual plotted against the corresponding iteration.

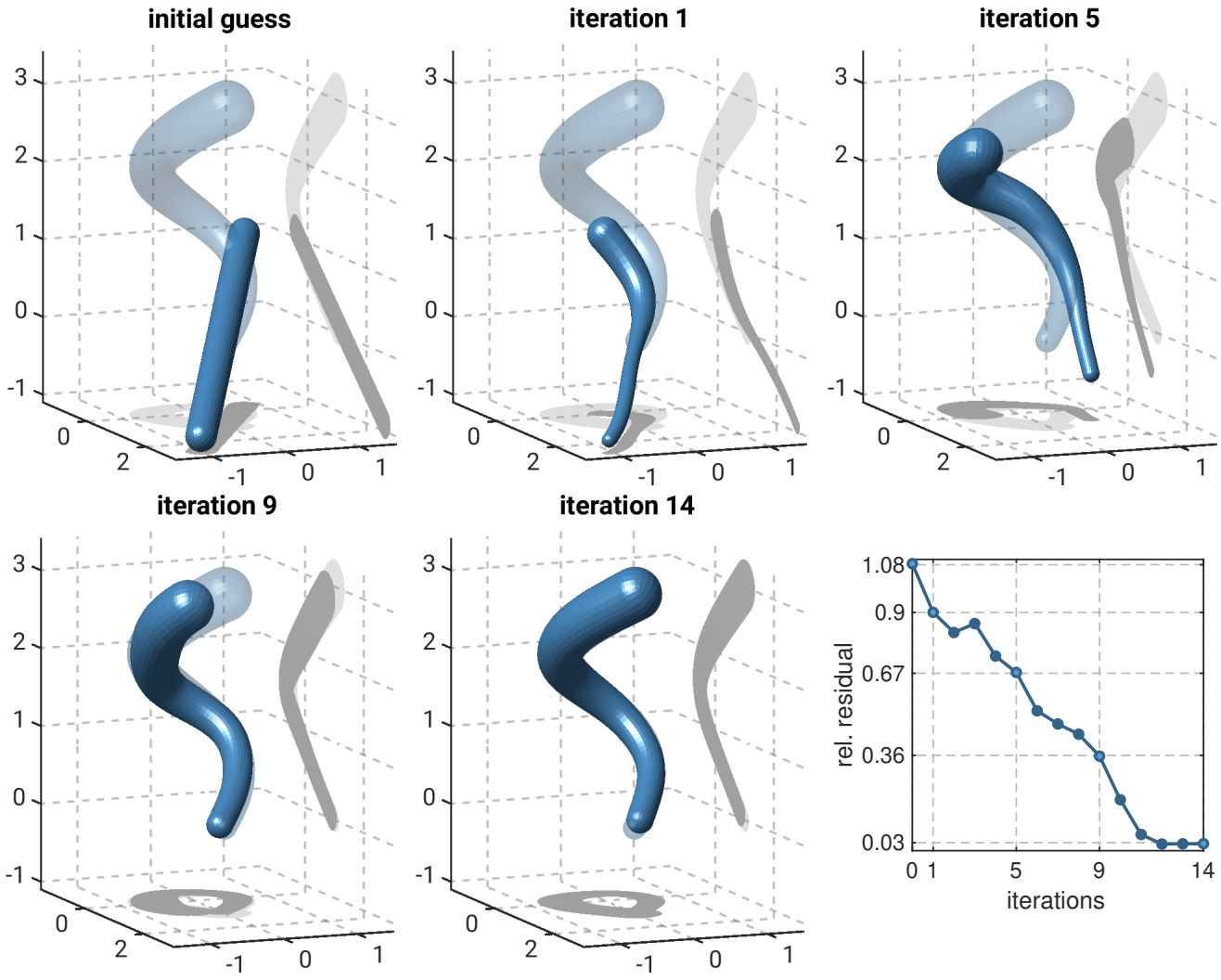

Figure 3: Top-left to bottom-center: The initial guess, samples of the reconstruction and the final reconstruction for Example 4.2 are depicted. The exact obstacle is displayed slightly transparent as a comparison for each iteration. Bottom-right: The relative residual plotted against the corresponding iteration.

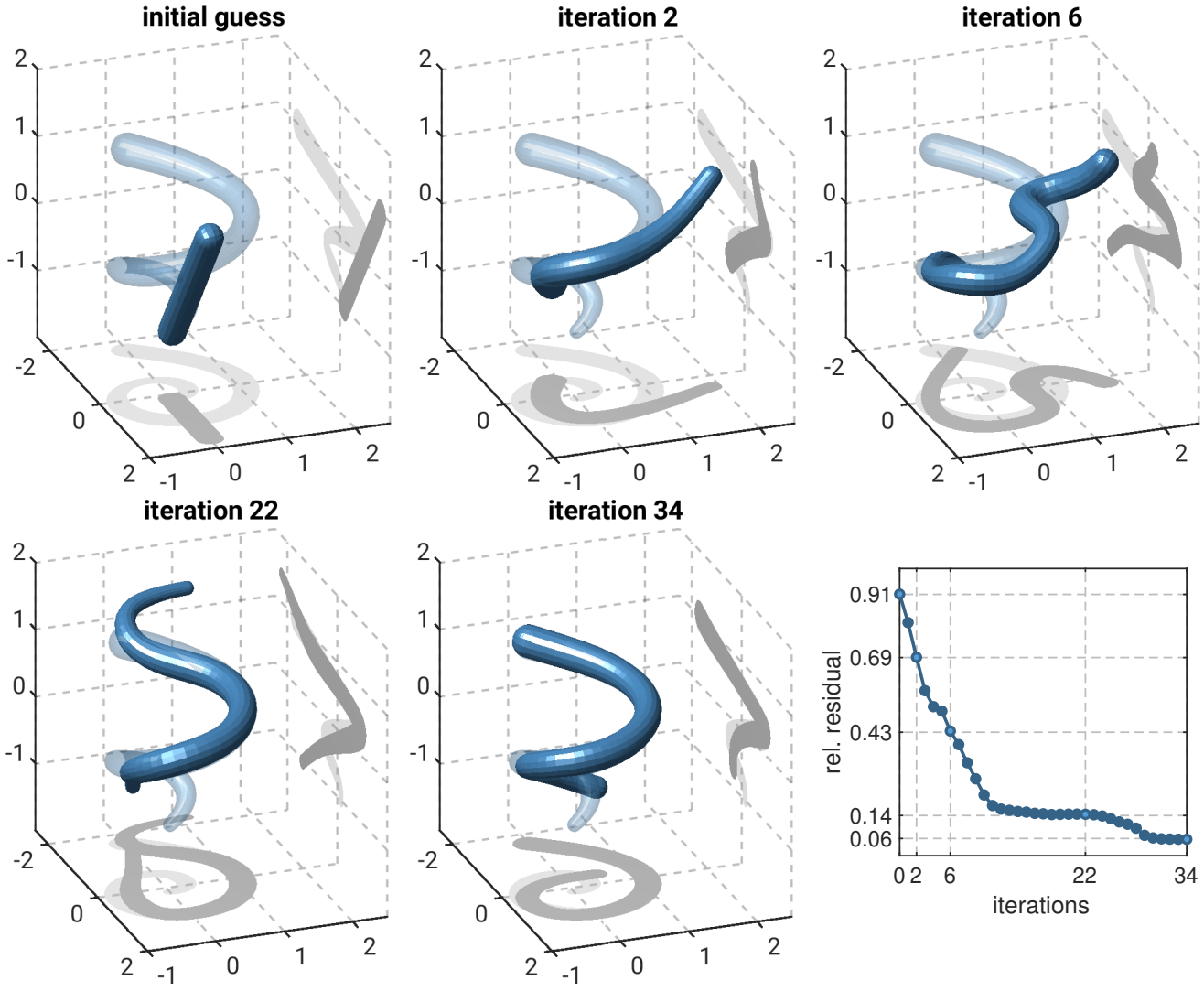

Figure 4: Top-left to bottom-center: The initial guess, samples of the reconstruction and the final reconstruction for Example 4.3 are depicted. The exact obstacle is displayed slightly transparent as a comparison for each iteration. Bottom-right: The relative residual plotted against the corresponding iteration.

functions with a total of 12852 *DOFs, respectively. The radius function of the initial guess is again chosen constant. We pick the regularization parameters* $\alpha_1 = 9/16$, $\alpha_2 = 64$, $\alpha_3 = 36$ *and start the reconstruction algorithm. Throughout the whole algorithm, the GMRES method approximating a solution to* (21) *converges within* 6 *to* 7 *iterations. Starting with a relative residual of approximately* 108.4% *the Gauss–Newton iteration terminates after* 14 *iterations with a relative residual of about* 2.6%. *In Figure 4 samples of the reconstruction are depicted.*

Example 4.3 *We consider a penetrable obstacle, where the material parameters are chosen as* $\varepsilon_1 = 2$, $\mu_1 = 3/2$, *i.e.,* $\varepsilon_r = 2$, $\mu_r = 3/2$, *and the angular frequency as* $\omega = 2\sqrt{2}$. *In this example,* $\boldsymbol{z}$ *is the* 3*rd-degree B-spline curve with control points* $\boldsymbol{c}_j = ((j/6+3/20)\cos(j\pi/3), (j/6+3/20)\sin(j\pi/3), 2j/9-1)^\top$, $j = 0, \dots, 9$. *This represents a conical helical object performing one and a half turns around the vertical axis. We consider the radius function* $r = 1/10\,\exp(\sin(\,\cdot\,)) + 1/30\,\sin(4\pi\,\cdot\,)$, *which is represented by a cubic spline with the distinct knots of the B-spline as the interpolation points. The finite element space of RWG and BC functions, which is used for computing the exact far field data, has* 9780 *DOFs in total.*

To represent the domains in the reconstruction, we use 12 *control points and the knots* $t_j = j/11$, $j = 0, \dots, 11$. *The finite element spaces of RWG and BC functions which are used throughout the iteration have* 6624 *DOFs in total. The radius function of the initial guess is again chosen constant. The regularization parameters are chosen as* $\alpha_1 = 9/25$, $\alpha_2 = 64$, $\alpha_3 = 16$. *The GMRES method approximating the solution to* (21) *converges within* 7 *to* 9 *iterations. The Gauss–Newton iteration starts with a relative residual of approximately* 91.1% *and terminates after* 34 *iterations with a relative residual of around* 5.7%. *In Figure 4 samples of the reconstruction are depicted. Restarting the algorithm with the final reconstruction seen in the bottom middle plot of Figure 4 as the initial guess, but with the regularization parameters lowered to* $\alpha_1 = 1/100$, $\alpha_2 = 1$, $\alpha_3 = 1/4$, *yields an even better result with a relative residual of around* 1.8% *after* 5 *additional iterations. We do not show this result graphically here.*

The examples show that we have developed an algorithm that reliably reconstructs the shape of tubular scatterers from electromagnetic far field patterns for just one incident plane wave. In all cases, we obtain a very good approximation of both the spine curve and the radius function. In our experiments, the most delicate issue has turned out to be the choice of regularization parameters for which we cannot offer an automated or a-posteriori selection procedure. A reasonable choice leads to a very good approximation of the scatterers shape in all examples. For challenging geometries, in particular such as in example 4.3, the stopping criterion of small updates in the iteration is met rather than that of the relative residual falling below the noise level in the data. In such cases, a restart of the minimization with reduced regularization parameters, as outlined at the end of example 4.3, often yields an additional improvement of the shape approximation.

We observe that the reconstruction of penetrable obstacles with real permitivitties and permeabilities works more reliably and stably than the reconstruction of perfectly conducting obstacles. For objects with a helical structure, it has turned out to be quite delicate to reconstruct perfect conductors with more than 1/2 turns while this is still soundly feasible for dielectric scatterers.

In conclusion, we derived a computable characterization of the domain derivative of far fields for a class of tubular objects, where – in contrast to star-shaped obstacles – the surface representation depends non-linearly on the degrees of freedom in the parameterization. Furthermore, we have demonstrated consistent reconstructions of a variety of such objects, confirming the underlying theoretical results.

Acknowledgments

Funded by the Deutsche Forschungsgemeinschaft (DFG, German Research Foundation) – Project-ID 258734477 – SFB 1173.

References

[1] T. Arens, R. Griesmaier, and M. Knöller. Maximizing the electromagnetic chirality of thin dielectric tubes. *SIAM J. Appl. Math.*, 81(5):1979–2006, 2021. doi:10.1137/21M1393509.

[2] A. Buffa, M. Costabel, and D. Sheen. On traces for $\mathbf{H}(\mathbf{curl}, \Omega)$ in Lipschitz domains. *J. Math. Anal. Appl.*, 276(2):845–867, 2002. doi:10.1016/S0022-247X(02)00455-9.

[3] A. Buffa and R. Hiptmair. Galerkin boundary element methods for electromagnetic scattering. *Topics in Computational Wave Propagation, Lect. Notes Comput. Sci. Eng*, 31:85–126, 01 2003. doi:10.1007/978-3-642-55483-4_3.

[4] A. Buffa, R. Hiptmair, T. v. Petersdorff, and C. Schwab. Boundary element methods for Maxwell transmission problems in Lipschitz domains. *Numer. Math.*, 95(3):459–485, 2003. doi:10.1007/s00211-002-0407-z.

[5] Y. Capdeboscq, R. Griesmaier, and M. Knöller. An asymptotic representation formula for scattering by thin tubular structures and an application in inverse scattering. *Multiscale Model. Simul.*, 19(2):846–885, 2021. doi:10.1137/20M1369907.

[6] H. Contopanagos, B. Dembart, M. Epton, J. J. Ottusch, V. Rokhlin, J. L. Visher, and S. M. Wandzura. Well-conditioned boundary integral equations for three-dimensional electromagnetic scattering. *IEEE Trans. Antennas Propag.*, 50(12):1824–1830, 2002. doi:10.1109/TAP.2002.803956.

[7] I. Fernandez-Corbaton, M. Fruhnert, and C. Rockstuhl. Objects of maximum electromagnetic chirality. *Phys. Rev. X*, 6(3), 2016. doi:10.1103/physrevx.6.031013.

[8] I. Fernandez-Corbaton, R. Griesmaier, M. Knöller, and C. Rockstuhl. Maximizing the electromagnetic chirality of thin metallic nanowires at optical frequencies. *J. Comput. Phys.*, 475:111854, 23, 2023. doi:10.1016/j.jcp.2022.111854.

[9] J. K. Gansel, M. Wegener, S. Burger, and S. Linden. Gold helix photonic metamaterials: A numerical parameter study. *Opt. Express*, 18(2):1059–1069, 2010. doi:10.1364/OE.18.001059.

[10] X. Garcia-Santiago, M. Hammerschmidt, J. Sachs, S. Burger, H. Kwon, M. Knöller, T. Arens, P. Fischer, I. Fernandez-Corbaton, and C. Rockstuhl. Toward maximally electromagnetically chiral scatterers at optical frequencies. *ACS Photonics*, 9(6):1954–1964, 2022. doi:10.1021/acsphotonics.1c01887.

[11] R. Griesmaier and N. Hyvönen. A regularized newton method for locating thin tubular conductivity inhomogeneities. *Inverse Problems*, 27(11):115008, 2011. doi:10.1088/0266-5611/27/11/115008.

[12] F. Hagemann, T. Arens, T. Betcke, and F. Hettlich. Solving inverse electromagnetic scattering problems via domain derivatives. *Inverse Problems*, 35(8):084005, 2019. doi:10.1088/1361-6420/ab10cb.

[13] F. P. Hagemann. *Reconstructing the Shape and Measuring Chirality of Obstacles in Electromagnetic Scattering*. PhD thesis, Karlsruher Institut für Technologie (KIT), 2019. doi:10.5445/IR/1000100295.

[14] F. Hettlich. The domain derivative of time-harmonic electromagnetic waves at interfaces. *Math. Methods Appl. Sci.*, 35(14):1681–1689, 2012. doi:10.1002/mma.2548.

[15] A. Kirsch. The domain derivative and two applications in inverse scattering theory. *Inverse Problems*, 9(1):81–96, 1993. doi:10.1088/0266-5611/9/1/005.

[16] M. Knöller. *Electromagnetic scattering from thin tubular objects and an application in electromagnetic chirality*. PhD thesis, Karlsruher Institut für Technologie (KIT), 2023. doi:10.5445/IR/1000161368.

[17] R. A. Litherland, J. Simon, O. Durumeric, and E. Rawdon. Thickness of knots. *Topology Appl.*, 91(3):233–244, 1999. doi:10.1016/S0166-8641(97)00210-1.

[18] P. Monk. *Finite element methods for Maxwells equations*. Numerical mathematics and scientific computation, Oxford science publications. Clarendon Press, Oxford, 1st edition, 2003. doi:10.1093/acprof:oso/9780198508885.001.0001.

[19] R. Potthast. Domain derivatives in electromagnetic scattering. *Math. Methods Appl. Sci.*, 19(15):1157–1175, 1996. doi:10.1002/(SICI)1099-1476(199610)19:15<1157::AID-MMA814>3.3.CO;2-P.

[20] M. W. Scroggs, T. Betcke, E. Burman, W. Śmigaj, and E. van 't Wout. Software frameworks for integral equations in electromagnetic scattering based on Calderón identities. *Comput. Math. Appl.*, 74(11):2897–2914, 2017. doi:10.1016/j.camwa.2017.07.049.

[21] W. Wang, B. Jüttler, D. Zheng, and Y. Liu. Computation of rotation minimizing frames. *ACM Trans. Graph.*, 27:Article 2, 2008. doi:10.1145/1330511.1330513.

A Proof of Lemma 3.3

We here give the proof of Lemma 3.3. Obviously, $\boldsymbol{x}_{\text{body}}$, $\boldsymbol{x}_{\text{start}}$ and $\boldsymbol{x}_{\text{end}}$ each are parametrizations of C^1-smooth surface patches in $\mathbb{R}^3$. Moreover,

$$\boldsymbol{x}_{\text{end}}(\tfrac{\pi}{2},\varphi) \;=\; \boldsymbol{z}(1) + \rho_1(\tfrac{\pi}{2},\varphi)\,\boldsymbol{\zeta}(1,\varphi) \;=\; \boldsymbol{z}(1) + r(1)\,\boldsymbol{\zeta}(1,\varphi) \;=\; \boldsymbol{x}_{\text{body}}(1,\varphi)\,,$$

and

$$\begin{aligned}\boldsymbol{x}_{\text{start}}(\tfrac{\pi}{2},\varphi) \;&=\; \boldsymbol{z}(0) + \rho_0(\tfrac{\pi}{2},\varphi)\,(\cos(\varphi)\,\boldsymbol{b}(0) + \sin(\varphi)\,\boldsymbol{n}(0))\\ &=\; \boldsymbol{z}(0) + \rho_0(\tfrac{\pi}{2},\varphi)\,\big(\sin(\tfrac{\pi}{2}-\varphi)\,\boldsymbol{b}(0) + \cos(\tfrac{\pi}{2}-\varphi)\,\boldsymbol{n}(0)\big)\\ &=\; \boldsymbol{z}(0) + r(0)\,\boldsymbol{\zeta}(0,\tfrac{\pi}{2}-\varphi) \;=\; \boldsymbol{x}_{\text{body}}(0,\tfrac{\pi}{2}-\varphi)\,.\end{aligned}$$

Hence, these three functions form the atlas of a C^0-smooth surface. Note that the φ-coordinate is oriented differently for the starting cap than for the body and end cap, and that there is a phase-shift.

It remains to show that the unit normal is continuous across the interfaces of the three surface patches. By Lemma 3.2,

$$\partial_\varphi \boldsymbol{x}_{\text{body}} \times \partial_\tau \boldsymbol{x}_{\text{body}} \;=\; r\,\partial_\varphi\boldsymbol{\zeta} \times (\psi\,\boldsymbol{t} + r'\,\boldsymbol{\zeta}) \;=\; r\,(\psi\,\partial_\varphi\boldsymbol{\zeta} \times \boldsymbol{t} + r'\partial_\varphi\boldsymbol{\zeta} \times \boldsymbol{\zeta})\,.$$

We note that

$$\partial_\vartheta\rho_1(\tfrac{\pi}{2},\varphi) \;=\; -\frac{r(1)\,r'(1)}{\psi(1,\varphi)}\,, \qquad \partial_\varphi\rho_1(\tfrac{\pi}{2},\varphi) \;=\; 0\,.$$

Hence,

$$\begin{aligned}\partial_\vartheta\boldsymbol{x}_{\text{end}}(\tfrac{\pi}{2},\varphi) \;&=\; \partial_\vartheta\rho_1(\tfrac{\pi}{2},\varphi)\,\boldsymbol{\xi}_{\text{end}}(\tfrac{\pi}{2},\varphi) + \rho_1(\tfrac{\pi}{2},\varphi)\,\partial_\vartheta\boldsymbol{\xi}_{\text{end}}(\tfrac{\pi}{2},\varphi)\\ &=\; -\frac{r(1)\,r'(1)}{\psi(1,\varphi)}\,(\cos(\varphi)\,\boldsymbol{n}(1) + \sin(\varphi)\,\boldsymbol{b}(1)) - r(1)\,\boldsymbol{t}(1)\\ &=\; -\frac{r(1)}{\psi(1,\varphi)}\,(r'(1)\,\boldsymbol{\zeta}(1,\varphi) + \psi(1,\varphi)\,\boldsymbol{t}(1))\,,\\ \partial_\varphi\boldsymbol{x}_{\text{end}}(\tfrac{\pi}{2},\varphi) \;&=\; \partial_\varphi\rho_1(\tfrac{\pi}{2},\varphi)\,\boldsymbol{\xi}_{\text{end}}(\tfrac{\pi}{2},\varphi) + \rho_1(\tfrac{\pi}{2},\varphi)\,\partial_\varphi\boldsymbol{\xi}_{\text{end}}(\tfrac{\pi}{2},\varphi)\\ &=\; r(1)\,(-\boldsymbol{n}(1)\,\sin(\varphi) + \boldsymbol{b}(1)\cos(\varphi)) \;=\; r(1)\,\partial_\varphi\boldsymbol{\zeta}(1,\varphi)\,.\end{aligned}$$

We conclude from

$$\begin{aligned}\partial_\vartheta\boldsymbol{x}_{\text{end}}(\tfrac{\pi}{2},\varphi) \times \partial_\varphi\boldsymbol{x}_{\text{end}}(\tfrac{\pi}{2},\varphi) \;&=\; -\frac{r(1)^2}{\psi(1,\varphi)}\,(\psi(1,\varphi)\,\boldsymbol{t}(1) + r'(1)\,\boldsymbol{\zeta}(1,\varphi)) \times \partial_\varphi\boldsymbol{\zeta}(1,\varphi)\\ &=\; \frac{r(1)}{\psi(1,\varphi)}\,(\partial_\varphi\boldsymbol{x}_{\text{body}}(1,\varphi) \times \partial_\tau\boldsymbol{x}_{\text{body}}(1,\varphi))\end{aligned}$$

that the unit normal vector is continuous across the interface of S_{body} and S_{end}.

Completely analogously, we have

$$\partial_\vartheta\rho_0(\tfrac{\pi}{2},\varphi) \;=\; -\frac{r(0)\,r'(0)}{\psi(0,\frac{\pi}{2}-\varphi)}\,, \qquad \partial_\varphi\rho_0(\tfrac{\pi}{2},\varphi) \;=\; 0\,,$$

and thus

$$\begin{aligned}\partial_\vartheta \boldsymbol{x}_{\text{start}}(\tfrac{\pi}{2},\varphi) &= -\frac{r(0)}{\psi(0,\frac{\pi}{2}-\varphi)}\left(r'(0)\,\boldsymbol{\zeta}(0,\tfrac{\pi}{2}-\varphi)+\psi(0,\tfrac{\pi}{2}-\varphi)\,\boldsymbol{t}(0)\right),\\ \partial_\varphi \boldsymbol{x}_{\text{start}}(\tfrac{\pi}{2},\varphi) &= r(0)\,\partial_\varphi\boldsymbol{\zeta}(0,\tfrac{\pi}{2}-\varphi).\end{aligned}$$

Hence

$$\begin{aligned}&\partial_\vartheta \boldsymbol{x}_{\text{start}}(\tfrac{\pi}{2},\varphi)\times\partial_\phi \boldsymbol{x}_{\text{start}}(\tfrac{\pi}{2},\varphi)\\ &\qquad = \frac{r(0)}{\psi(0,\frac{\pi}{2}-\varphi)}\left(\partial_\varphi \boldsymbol{x}_{\text{body}}(1,\tfrac{\pi}{2}-\varphi)\times\partial_\tau \boldsymbol{x}_{\text{body}}(1,\tfrac{\pi}{2}-\varphi)\right),\end{aligned}$$

establishing that the unit normal vector is also continuous across the interface of S_{body} and S_{start}.

B Proof of Lemma 3.6

We use the linearization formulas

$$\frac{1}{x+h} = \frac{1}{x}-\frac{h}{x^2}+\mathrm{o}(h), \quad h\to 0, \qquad \frac{1}{|\boldsymbol{x}+\boldsymbol{h}|} = \frac{1}{|\boldsymbol{x}|}-\frac{\boldsymbol{x}\cdot\boldsymbol{h}}{|\boldsymbol{x}|^3}+\mathrm{o}(|\boldsymbol{h}|), \quad \boldsymbol{h}\to 0.$$

The second formula gives

$$\begin{aligned}\boldsymbol{t}'_{\boldsymbol{\delta}} &= \frac{\boldsymbol{z}''_{\boldsymbol{\delta}}}{|\boldsymbol{z}'_{\boldsymbol{\delta}}|}-\frac{\boldsymbol{t}_{\boldsymbol{\delta}}\cdot\boldsymbol{z}''_{\boldsymbol{\delta}}}{|\boldsymbol{z}'_{\boldsymbol{\delta}}|}\,\boldsymbol{t}_{\boldsymbol{\delta}} = \boldsymbol{t}'+\frac{1}{|\boldsymbol{z}'|}\left(\boldsymbol{\delta}''-(\boldsymbol{\delta}''\cdot\boldsymbol{t})\,\boldsymbol{t}\right)-\frac{\boldsymbol{\delta}'\cdot\boldsymbol{t}}{|\boldsymbol{z}'|^2}\left(\boldsymbol{z}''-(\boldsymbol{z}''\cdot\boldsymbol{t})\,\boldsymbol{t}\right)\\ &\quad-\frac{\boldsymbol{z}''\cdot\boldsymbol{t}}{|\boldsymbol{z}'|^2}\left(\boldsymbol{\delta}'-(\boldsymbol{\delta}'\cdot\boldsymbol{t})\,\boldsymbol{t}\right)-\frac{\boldsymbol{z}''}{|\boldsymbol{z}'|^2}\cdot\left(\boldsymbol{\delta}'-(\boldsymbol{\delta}'\cdot\boldsymbol{t})\,\boldsymbol{t}\right)\boldsymbol{t}+\mathrm{o}\left(\|\boldsymbol{\delta}\|_{2,\infty}\right) \qquad \|\boldsymbol{\delta}\|_{2,\infty}\to 0.\end{aligned}$$

From the asymptotic expansions in (11), from (12a) and $\boldsymbol{t}'\cdot\boldsymbol{t}=0$, we have

$$\boldsymbol{t}'_{\boldsymbol{\delta}}\cdot\boldsymbol{\zeta}_{\boldsymbol{\delta}} = \left(\boldsymbol{t}'+\frac{1}{|\boldsymbol{z}'|}\,\boldsymbol{\delta}''-\frac{\boldsymbol{\delta}'\cdot\boldsymbol{t}}{|\boldsymbol{z}'|^2}\,\boldsymbol{z}''-\frac{\boldsymbol{z}''\cdot\boldsymbol{t}}{|\boldsymbol{z}'|^2}\,\boldsymbol{\delta}'\right)\cdot\boldsymbol{\zeta}+\mathrm{o}\left(\|\boldsymbol{\delta}\|_{2,\infty}\right) \qquad (\|\boldsymbol{\delta}\|_{2,\infty}\to 0).$$

Hence, from (14) we obtain the asserted asymptotic perturbation formula for $\psi_{\boldsymbol{\delta}}$. By inserting this expansion in (15) and using the first linearization formula, we obtain

$$\begin{aligned}\rho_{1,(\boldsymbol{\delta},\varepsilon)} &= \rho_1+\left(1-\frac{\eta_1}{r(1)}-\frac{\eta_1}{\psi(1,\cdot)}\boldsymbol{t}'(1)\cdot\boldsymbol{\zeta}(1,\cdot)\right)\varepsilon(1)-\frac{1}{r'(1)}\,\eta_1\,\varepsilon'(1)\\ &\quad+\frac{\eta_1}{\psi(1,\cdot)}\left(\boldsymbol{t}(1)\cdot\boldsymbol{\delta}'(1)+r(1)\left(\frac{\boldsymbol{z}''(1)\cdot\boldsymbol{\zeta}(1,\cdot)}{|\boldsymbol{z}'(1)|^2}\,\boldsymbol{t}(1)+\frac{\boldsymbol{z}''(1)\cdot\boldsymbol{t}(1)}{|\boldsymbol{z}'(1)|^2}\,\boldsymbol{\zeta}(1,\cdot)\right)\cdot\boldsymbol{\delta}'(1)\right.\\ &\quad\left.-\frac{r(1)}{|\boldsymbol{z}'(1)|}\,\boldsymbol{\zeta}(1,\cdot)\cdot\boldsymbol{\delta}''(1)\right)+\mathrm{o}\left(\|\boldsymbol{\delta}\|_{2,\infty}+\|\varepsilon\|_{1,\infty}\right) \qquad \|\boldsymbol{\delta}\|_{2,\infty}\to 0,\ \|\varepsilon\|_{1,\infty}\to 0.\end{aligned}$$

This is the asserted asymptotic perturbation formula for ρ_1. The formula for ρ_0 is obtained analogously.

Finally, from the asymptotic expansions in (11a) we directly obtain the asymptotic expressions for $\boldsymbol{\xi}_{\text{start}}$ and $\boldsymbol{\xi}_{\text{end}}$.